NASA Contractor Report 4308

Development of a Linearized Unsteady Aerodynamic Analysis for Cascade Gust Response Predictions

Joseph M. Verdon and Kenneth C. Hall

NASA

NASA Contractor Report 4308

Development of a Linearized Unsteady Aerodynamic Analysis for Cascade Gust Response Predictions

Joseph M. Verdon and Kenneth C. Hall
United Technologies Research Center
East Hartford, Connecticut

NASA

National Aeronautics and
Space Administration

Office of Management

Scientific and Technical
Information Division

1990

Contents

Preceding Page Blank

Development of a Linearized Unsteady Aerodynamic Analysis for Cascade Gust Response Predictions

Summary

A method for predicting the unsteady aerodynamic response of a cascade of airfoils to entropic, vortical, and acoustic gust excitations is being developed. Here, the unsteady flow is regarded as a small perturbation of a nonuniform isentropic and irrotational steady background flow. A splitting technique is used to decompose the linearized unsteady velocity into rotational and irrotational parts leading to equations for the complex amplitudes of the linearized unsteady entropy, rotational velocity, and velocity potential that are coupled only sequentially. The entropic and rotational velocity fluctuations are described by transport equations for which closed-form solutions in terms of the mean-flow drift and stream functions can be determined. The potential fluctuation is described by an inhomogeneous convected wave equation in which the source term depends on the rotational velocity field, and is determined using finite-difference procedures. In this report the analytical and numerical techniques used to determine the linearized unsteady flow are outlined. Results are presented to indicate the status of the solution procedure and to demonstrate the impact of blade geometry and mean blade loading on the aerodynamic response of cascades to vortical gust excitations. The analysis described herein leads to very efficient predictions of cascade unsteady aerodynamic response phenomena making it useful for turbomachinery aeroelastic and aeroacoustic design applications.

1. Introduction

Destructive forced vibrations can occur in turbomachinery blading when a periodic aerodynamic force, with frequency close to a system natural frequency, acts on the blades. A primary source of such vibrations is the aerodynamic interactions between adjacent blade rows, of which the two principal types are traditionally referred to as potential-flow interaction and wake interaction. The former results from the variations in the velocity potential or pressure field associated with the blades of a given row and their effect on the blades of a neighboring row moving at a different rotational speed. This type of interaction is of serious concern when the axial spacings between neighboring blade rows are small or flow Mach numbers are high. Wake interaction is the effect upon the flow through a blade row of the wakes shed by one or more upstream rows. This type of interaction can persist over considerable axial distances.

The theoretical unsteady aerodynamic analyses that have been developed to predict the aeroelastic behavior of turbomachinery blading, i.e., the onset of blade flutter and the amplitudes of forced blade vibration, have, for the most part, been based on the following simplifying assumptions: the blades of an isolated two-dimensional cascade are considered and the effects of neighboring structures are represented via nonuniform inlet and exit conditions, viscous effects are usually neglected, and the unsteady fluctuations are assumed to be sufficiently small so that a linearized treatment of the unsteady flow is justified. Then, to determine the aeroelastic characteristics of the blading, the resulting analyses must be capable of predicting the unsteady loads that act on the blades and arise from various sources of excitation, i.e., prescribed structural (blade) motions and external aerodynamic excitations. The latter include variations in total temperature and total pressure (entropy and vorticity waves) at inlet and variations in static pressure (acoustic waves) at inlet and exit. In particular, for blade flutter applications it is only necessary to predict the unsteady loads resulting from prescribed blade motions, while for forced response applications the unsteady loads due to incident entropic, vortical and acoustic disturbances are also required.

Until recently, the unsteady aerodynamic analyses that have been available for turbomachinery aeroelastic applications were based on classical linearized theory (for an informative review see Whitehead Ref. [1]). Here, the steady and first-harmonic unsteady departures of the flow variables from their uniform free-stream values are regarded as small and of the same order of magnitude leading to uncoupled, linear, constant-coefficient boundary-value problems for the steady and unsteady disturbances. Thus, unsteady solutions based on the classical linearization are essentially restricted to cascades of unloaded flat-plate blades which operate in an entirely subsonic or an entirely supersonic environment. Very efficient semi-analytic solution procedures have been developed for two-dimensional attached subsonic [2–4] and supersonic [5–8] flows and applied with some success in turbomachinery aeroelastic (and aeroacoustic) design calculations. It should also be mentioned that extensive efforts, as reviewed in Ref. [9], have been made to develop three-dimensional unsteady aerodynamic analyses based on the classical linearization for turbomachinery aeroelastic and aeroacoustic design applications.

Because of the limitations in physical modeling associated with the classical linearization, more general two-dimensional inviscid linearizations are being developed [10–12]. These

account for the effects of important design features such as real blade geometry, mean blade loading and operation at transonic Mach numbers on the unsteady aerodynamic response of a cascade. Here, unsteady disturbances are regarded as small-amplitude harmonic fluctuations relative to a nonuniform steady (in a coordinate frame attached to the blade row) background flow. The steady flow is determined as a solution of a nonlinear inviscid equation set, and the unsteady flow is governed by a set of linear equations with variable coefficients that depend on the underlying steady flow. This type of analytical model has received considerable attention in recent years, and we refer the reader to the recent review articles by Verdon [13,14] for a detailed description of the theoretical formulation. Useful solution algorithms for the nonlinear steady problem are currently available, and solution methods [15] for linearized unsteady perturbations of isentropic and irrotational background flows have reached the stage where it is appropriate to consider them for design applications. Unfortunately, such methods have, for the most part, only been developed for the prediction of unsteady flows driven by prescribed blade vibrations and/or incident acoustic disturbances. Recently, Hall and Crawley [12] used the linearized Euler equations to describe unsteady cascade flows caused by wake (entropic and vortical) excitations. A linearized Euler technique, while needed to account for strong shock and rotational mean flow phenomena, is not as efficient as a linearization based on the isentropic and irrotational mean flow assumptions.

Thus, under the present effort, an analysis and computer code (LINFLO) has been developed to predict linearized unsteady cascade flows containing entropic and vortical, as well as acoustic, perturbations of isentropic and irrotational mean or steady flows. In this analysis the Goldstein velocity decomposition [16,17] is employed to split the linearized unsteady velocity into rotational and irrotational components. This decomposition leads to a very convenient description of the linearized unsteady perturbation — one in which the equations that govern the entropy, rotational velocity and velocity potential fluctuations are coupled only sequentially. In addition, closed form solutions can be determined for the entropy and rotational velocity fluctuations in terms of the drift and stream functions of the underlying steady flow. Finally, the unsteady potential is governed by an inhomogeneous wave equation in which the source term depends only upon the rotational velocity field. Finite-difference solution procedures for this equation are already available [18,19]. The Goldstein splitting introduces singularities in the rotational and irrotational unsteady velocities along the surfaces of blades and their wakes. Thus, a modification introduced by Atassi and Grzedzinski [20] has been employed in the present analysis to remove the singular behavior, thereby permitting an accurate numerical evaluation of the entropy and rotational velocity fluctuations and an accurate numerical resolution of the wave equation that governs the unsteady velocity potential.

The linearized unsteady aerodynamic analysis is described in this report and demonstrated via application to a number of representative cascade configurations. It has been implemented into an existing computer code LINFLO, which can be used to predict the pressure response of realistic cascade configurations to prescribed external aerodynamic (i.e., incident entropic, vortical and acoustic disturbances) and structural (blade motions) excitations. Because it permits a very efficient and economical prediction of cascade response to aerodynamic and structural excitations, the LINFLO code is suitable for implementation into turbomachinery aeroelastic and aeroacoustic design prediction systems.

3

2. Physical Problem

We consider the time-dependent adiabatic flow, with negligible body forces, of an inviscid non-heat-conducting perfect gas through a two-dimensional cascade such as the one shown in Figure 1. The mean or steady-state positions of the blade chord lines coincide with the line segments $\eta = \xi \tan\Theta + mG, 0 \le \xi \le \cos\Theta$, $m = 0$, ± 1, ± 2, ..., where ξ and η are coordinates in the cascade axial and circumferential directions, respectively, m is a blade number index, Θ is the cascade stagger angle, and $\mathbf{G}$ is the cascade gap vector which is directed along the η-axis with magnitude equal to the blade spacing. In the present discussion all physical quantities are dimensionless. Lengths are scaled with respect to blade chord, time with respect to the ratio of blade chord to upstream free-stream flow speed, density and velocity with respect to upstream free-stream density and flow speed, respectively, pressure with respect to the product of the upstream free-stream density and the square of the upstream free-stream speed, and entropy with respect to the specific heat of the fluid at constant pressure.

The time-dependent or unsteady fluctuations in the flow can arise from one or more of the following sources (Figure 2): blade motions, upstream and/or downstream acoustic disturbances which carry energy toward the blade row, and upstream entropic and vortical disturbances which are convected through the blade row. These excitations are each assumed to be of small amplitude, periodic in time and to occur at temporal frequency ω. The external aerodynamic excitations are also spatially periodic, while the structural excitation is periodic in the cascade circumferential or η-direction. For example, we consider blade motions of the form

$$\mathcal{R}(\mathbf{x} + m\mathbf{G}, t) = Re\{\mathbf{r}(\mathbf{x})\exp[i(\omega t + m\sigma)]\}, \quad \mathbf{x} \, \epsilon \, B \,, \tag{2.1}$$

where $\mathcal{R}$ measures the displacement of a point on a moving blade surface relative to its mean or steady-state position, $\mathbf{x}$ is a position vector, t is time, $\mathbf{r}$ is a complex displacement-amplitude vector, σ is the phase angle between the motions of adjacent blades, $Re\{\ \}$ denotes the real part of $\{\ \}$ and B denotes the reference ($m = 0$) blade surface. Incident disturbances are of the form

$$\tilde{s}(\mathbf{x}, t) = Re\{s_{-\infty}\exp[i(\boldsymbol{\kappa}_{-\infty} \cdot \mathbf{x} + \omega t)]\}, \quad \xi < \xi_- \,, \tag{2.2}$$

$$\tilde{\boldsymbol{\zeta}}(\mathbf{x}, t) = Re\{\boldsymbol{\zeta}_{-\infty}\exp[i(\boldsymbol{\kappa}_{-\infty} \cdot \mathbf{x} + \omega t)]\}, \quad \xi < \xi_- \,, \tag{2.3}$$

and

$$\tilde{p}_I(\mathbf{x}, t) = Re\{p_{I,\mp\infty}\exp[i(\boldsymbol{\kappa}_{\mp\infty} \cdot \mathbf{x} + \omega t)]\}, \quad \xi \lessgtr \xi_\mp \,. \tag{2.4}$$

Here $s_{-\infty}$, $\boldsymbol{\zeta}_{-\infty}$ and $p_{I,\mp\infty}$ are the complex amplitudes of the incident entropic, vortical and pressure fluctuations, $\tilde{s}(\mathbf{x}, t)$, $\tilde{\boldsymbol{\zeta}}(\mathbf{x}, t)$ and $\tilde{p}_I(\mathbf{x}, t)$, respectively, far upstream ($-\infty$) and far downstream ($+\infty$) from the blade row. The entropic and vortical excitations originate far upstream of the blade row ($\xi < \xi_-$); the incident pressure disturbances, $\tilde{p}_I(\mathbf{x}, t)$, originate far upstream and/or far downstream ($\xi > \xi_+$) and carry energy towards the blade row. We use the symbol $\boldsymbol{\kappa}$ to denote the wave number of an incident disturbance. The interblade phase angle, σ, of an incident disturbance is given by $\boldsymbol{\kappa}_{\mp\infty} \cdot \mathbf{G}$. Also, the temporal frequency and wave number of an incident entropic or vortical disturbance are related by $\omega = -\boldsymbol{\kappa}_{-\infty} \cdot \mathbf{V}_{-\infty}$, where $\mathbf{V}_{-\infty}$ is the uniform relative inlet velocity, but a more complicated relationship exists between ω and $\boldsymbol{\kappa}_{-\infty}$ for an incident pressure disturbance (e.g., see [21]). In the present

investigation we are concerned primarily with determining the unsteady pressure response of cascades subjected to incident entropic and vortical excitations.

In the absence of unsteady excitation the flow beyond some finite distance upstream (say $\xi < \xi_-$) from the blade row is assumed to be at most a small irrotational steady perturbation of a uniform free stream. In addition, we assume that the unsteady flow remains attached to the blade surfaces; therefore, thin vortex sheets or unsteady wakes emanate from the trailing edges and extend downstream. Finally, any shocks that might occur are assumed to be of weak to moderate strength and have small curvature. Thus, changes in the entropy and vorticity of a fluid particle as it passes through shocks are regarded as negligible.

The fluid motion is governed by differential forms of the mass, momentum and energy conservation laws for an inviscid perfect gas (i.e., the Euler equations) in regions where the flow variables are continuous and corresponding jump conditions at surfaces across which the flow variables are discontinuous, i.e., at vortex-sheet wakes and at shocks. In continuous regions the energy equation can be replaced by the requirement that the entropy following a fluid particle must remain constant. In addition to the foregoing field equations and jump conditions, the attached flow assumption requires that the unsteady flow must be tangential to the moving blade surfaces. Finally, information on the uniform inlet and exit flow conditions, the entropic and vortical fluctuations at inlet and the static pressure disturbances at inlet and exit that carry energy toward the blade row must be specified. The remaining steady and unsteady departures from the uniform inlet and exit conditions (i.e., steady pressure variations, entropic and vortical fluctuations at exit and unsteady pressure fluctuations due to outgoing acoustic waves) must be determined as part of the time-dependent solution.

The foregoing unsteady aerodynamic problem is a formidable one. It involves a system of nonlinear time-dependent partial differential equations along with conditions imposed on moving blade, wake and shock surfaces in which the instantaneous positions of the wakes and shocks must, in principle, be determined as part of the solution. Because of these features and the prohibitive computational expense that would be involved in obtaining the unsteady aerodynamic response information needed for turbomachinery aeroelastic response predictions, the usual approach is to examine limiting forms of the full governing equations with the intention of providing efficient theoretical analyses for predicting the onset of blade flutter and the amplitudes of the vibratory blade motions caused by external aerodynamic excitations. One such approach, in which the unsteady flow is regarded as a small perturbation of a nonuniform isentropic and irrotational mean flow, is described below.

3. Unsteady Perturbations of a Potential Mean Flow

For small amplitude unsteady excitations, i.e., $|s_{-\infty}|$, $|\zeta_{-\infty}|$, etc., $\sim \mathcal{O}(\epsilon) << 1$, the time-dependent flow can be regarded as being a small perturbation of an underlying nonlinear mean or steady background flow. Thus, for example, we can set

$$\tilde{\mathbf{V}}(\mathbf{x}, t) = \mathbf{V}(\mathbf{x}) + \tilde{\mathbf{v}}(\mathbf{x}, t) + \cdots , \tag{3.1}$$

where $\mathbf{V}(\mathbf{x})$ is the local mean velocity and $\tilde{\mathbf{v}}(\mathbf{x}, t)$ is the first-order (in ϵ) unsteady velocity. Then, as a consequence of our assumptions regarding shocks and the flow far upstream of the blade row, the background flow will be isentropic and irrotational; i.e., $\mathbf{V} = \boldsymbol{\nabla}\Phi$, where Φ is the steady velocity potential. The field equations that govern the underlying steady potential flow follow from the mass and momentum conservation laws and the isentropic relations for a perfect gas and are given by

$$\boldsymbol{\nabla} \cdot (\bar{\rho}\boldsymbol{\nabla}\Phi) = 0 \tag{3.2}$$

and

$$(M_{-\infty}A)^2 = \bar{\rho}^{\,\gamma-1} = (\gamma M_{-\infty}^2 P)^{(\gamma-1)/\gamma} = 1 - \frac{\gamma-1}{2}M_{-\infty}^2[(\boldsymbol{\nabla}\Phi)^2 - 1] , \tag{3.3}$$

where M, A, $\bar{\rho}$ and P are the local Mach number, speed of sound propagation, density and pressure, respectively, in the mean or steady background flow and γ is the specific heat ratio of the fluid.

Surface conditions for this zeroth-order or steady flow apply at the mean positions, B_m, W_m and $\mathrm{Sh}_{m,n}$, of the blade, wake and shock surfaces, where the subscript n refers to the nth shock associated with the mth blade. Blade mean positions are prescribed, but the mean wake, i.e., the stagnation streamlines downstream of the blade row, and shock positions must be determined as part of the steady solution. Since, by assumption, the flow remains attached to the blade surfaces, a flow tangency condition applies at such surfaces. In addition, mass and tangential momentum must be conserved across shocks, and the steady pressure and normal velocity component must be continuous across blade wakes.

Numerical procedures for determining two-dimensional steady potential flows through cascades have been developed extensively, e.g., see [22,23], particularly for flows with subsonic relative inlet and exit Mach numbers (i.e., $M_{\mp\infty} < 1$). In such calculations far-field boundary conditions are imposed at axial stations placed at finite distances upstream and downstream (i.e., at $\xi = \xi_{\mp}$) from the blade row, where linearized solutions describing the behavior of the steady potential can be matched to a nonlinear near-field solution. In addition, conditions are often imposed at blade edges (e.g., a Kutta condition at sharp trailing edges) in lieu of prescribing an inlet and/or an exit free-stream property. Finally the usual practice is to solve the conservative form of the mass-balance equation (3.2) throughout the entire fluid domain while allowing for a discontinuity in the velocity potential across arbitrary periodic lines which emanate from the blade trailing-edge points and extend downstream. Thus, the shock- and wake-jump conditions, mentioned above, are usually not imposed explicitly in such steady-flow calculations. Instead, shock phenomena are captured through the use of special differencing techniques; the wake conditions are satisfied implicitly because, in a two-dimensional steady potential flow, the fluid properties are continuous and differentiable across wakes. The mean wake and shock locations are determined *a posteriori* from the resulting steady solution.

6

3.1 Linearized Unsteady Equations

The field equations that govern the first-order unsteady perturbation of a nonlinear isentropic and irrotational steady flow are determined from the full nonlinear time-dependent mass, momentum and entropy-transport equations and the thermodynamic equation relating the entropy, pressure and density of a perfect gas. After performing some straightforward algebra (see [13,14]), we obtain a system of differential equations for the first-order entropy ($\tilde{s}$), velocity ($\tilde{\mathbf{v}}$) and pressure ($\tilde{p}$), respectively. These equations can be cast in a very convenient form by introducing the Goldstein velocity decomposition [16,17]. Thus, after setting $\tilde{\mathbf{v}} = \boldsymbol{\nabla}\tilde{\phi} + \tilde{\mathbf{v}}_R$, where the unsteady potential $\tilde{\phi}$ governs the unsteady pressure fluctuation through the relation $\tilde{p} = -\bar{\rho}\bar{D}\tilde{\phi}/Dt$ and the rotational velocity, $\tilde{\mathbf{v}}_R$, is divergence free far upstream of the blade row, i.e., $\boldsymbol{\nabla} \cdot \tilde{\mathbf{v}}_R = 0$ for $\xi < \xi_-$, we find that the field equations that govern the unsteady flow variables can be written in the form

$$\frac{\bar{D}\tilde{s}}{Dt} = 0 \tag{3.4}$$

$$\frac{\bar{D}}{Dt}(\tilde{\mathbf{v}}_R - \tilde{s}\boldsymbol{\nabla}\Phi/2) + [(\tilde{\mathbf{v}}_R - \tilde{s}\boldsymbol{\nabla}\Phi/2) \cdot \boldsymbol{\nabla}]\boldsymbol{\nabla}\Phi = 0 \tag{3.5}$$

and

$$\frac{\bar{D}}{Dt}\left(A^{-2}\frac{\bar{D}\tilde{\phi}}{Dt}\right) - \bar{\rho}^{-1}\boldsymbol{\nabla} \cdot (\bar{\rho}\boldsymbol{\nabla}\tilde{\phi}) = \bar{\rho}^{-1}\boldsymbol{\nabla} \cdot (\bar{\rho}\tilde{\mathbf{v}}_R) . \tag{3.6}$$

Here $\bar{D}/Dt = \partial/\partial t + \boldsymbol{\nabla}\Phi \cdot \boldsymbol{\nabla}$ is a mean flow convective derivative operator. In general, we require a solution to the foregoing system of field equations subject to the condition of flow tangency at blade surfaces, jump conditions across shocks and blade wakes that are based on the fluid-dynamic conservation laws, and appropriate conditions far upstream and far downstream from the blade row.

Surface Conditions

As a consequence of the small unsteady-disturbance approximation, conditions on the linearized unsteady perturbation at moving blade, shock and wake surfaces can be imposed at the mean positions of these surfaces, with the mean wake (W_m), i.e., the downstream stagnation streamlines, and shock ($\text{Sh}_{m,n}$) locations being determined from the nonlinear steady solution. In particular, the following conditions (see [13] and [14]) apply. The first-order flow tangency condition has the form

$$(\boldsymbol{\nabla}\tilde{\phi} + \tilde{\mathbf{v}}_R) \cdot \mathbf{n} = [\partial\mathcal{R}/\partial t + (\boldsymbol{\nabla}\Phi \cdot \boldsymbol{\tau})(\boldsymbol{\tau} \cdot \boldsymbol{\nabla})\mathcal{R} - (\mathcal{R} \cdot \boldsymbol{\nabla})\boldsymbol{\nabla}\Phi] \cdot \mathbf{n}, \quad \mathbf{x} \in B_m . \tag{3.7}$$

The wake-jump conditions require that the fluid pressure and the normal component of the fluid velocity be continuous across blade wakes, i.e.,

$$[\![\bar{D}\tilde{\phi}/Dt]\!] = 0, \quad \mathbf{x} \in W_m , \tag{3.8}$$

and

$$[\![\boldsymbol{\nabla}\tilde{\phi} + \tilde{\mathbf{v}}_R]\!] \cdot \mathbf{n} = 0, \quad \mathbf{x} \in W_m , \tag{3.9}$$

7

respectively. Finally, if we neglect changes in entropy and rotational velocity across shocks, the conservation laws for mass and tangential momentum yield the following linearized shock-jump conditions:

$$[\![\bar{\rho}(\boldsymbol{\nabla}\tilde{\phi} - A^{-2}\frac{\bar{D}\tilde{\phi}}{Dt}\boldsymbol{\nabla}\Phi)]\!] \cdot \mathbf{n} + [\![\bar{\rho}]\!]\tilde{\mathbf{v}}_R \cdot \mathbf{n} = [\![\bar{\rho}]\!][\partial/\partial t + (\boldsymbol{\nabla}\Phi \cdot \boldsymbol{\tau})\boldsymbol{\tau} \cdot \boldsymbol{\nabla}](\mathcal{R} \cdot \mathbf{n})$$

$$+ (\mathcal{R} \cdot \mathbf{n})\boldsymbol{\tau} \cdot \boldsymbol{\nabla}([\![\bar{\rho}]\!]\boldsymbol{\nabla}\Phi \cdot \boldsymbol{\tau}) , \mathbf{x} \in \mathrm{Sh}_{m,n}$$

(3.10)

and, for a shock that terminates in the fluid,

$$[\![\tilde{\phi}]\!] = -\mathcal{R} \cdot \mathbf{n}[\![\boldsymbol{\nabla}\Phi]\!] \cdot \mathbf{n} , \mathbf{x} \in \mathrm{Sh}_{m,n} .$$

(3.11)

Equations (3.10) and (3.11) provide two relations for determining the jump in the unsteady potential, $[\![\tilde{\phi}]\!]$, at the mean position of a shock and the shock displacement normal to the mean shock locus, $\mathcal{R} \cdot \mathbf{n}$. In the foregoing equations $\mathbf{n}$ and $\boldsymbol{\tau}$ are unit vectors normal and tangential, respectively, to a surface and directed such that $\mathbf{n} \times \boldsymbol{\tau}$ points out from the page; the symbol $[\![\ ]\!]$ indicates the jump or change in a quantity at a surface at which the flow variables are discontinuous.

Far-Field Conditions

We have assumed that the potential mean or steady flow is at most a small (i.e., of $\mathcal{O}(\epsilon)$) perturbation from a uniform stream both far upstream ($\xi < \xi_-$) and far downstream ($\xi > \xi_+$) from the blade row. Therefore, in these regions, the first-order (in ϵ) unsteady field equations can be reduced to constant coefficient equations for which general solutions can be determined analytically (see [21]). Corresponding particular solutions are then determined from prescribed inlet and exit information and by matching the far field analytical solutions to a near-field numerical solution. For example, it follows from (3.4) and (3.5) that the entropy and rotational velocity fluctuations far upstream ($\xi < \xi_-$) and far downstream ($\xi > \xi_+$) of the blade row must be of the general form

$$\tilde{s}(\mathbf{x}, t) = \tilde{s}_{\mp\infty}(\mathbf{x} - \mathbf{V}_{\mp\infty}t), \quad \xi \gtrless \xi_\mp$$

(3.12)

and

$$\tilde{\mathbf{v}}_R(\mathbf{x}, t) = \tilde{\mathbf{v}}_{R,\mp\infty}(\mathbf{x} - \mathbf{V}_{\mp\infty}t), \quad \xi \gtrless \xi_\mp .$$

(3.13)

The far upstream entropy and rotational velocity fluctuations are prescribed, c.f. (2.2) and (2.3), and therefore

$$\tilde{s}(\mathbf{x}, t) = \tilde{s}_{-\infty}(\mathbf{x} - \mathbf{V}_{-\infty}t) = Re\{s_{-\infty} \exp[i\boldsymbol{\kappa}_{-\infty} \cdot (\mathbf{x} - \mathbf{V}_{-\infty}t)]\}, \quad \text{for} \quad \xi < \xi_- ,$$

(3.14)

and

$$\tilde{\mathbf{v}}_R(\mathbf{x}, t) = \tilde{\mathbf{v}}_{R,-\infty}(\mathbf{x} - \mathbf{V}_{-\infty}t) = Re\{\mathbf{v}_{R,-\infty} \exp[i\boldsymbol{\kappa}_{-\infty} \cdot (\mathbf{x} - \mathbf{V}_{-\infty}t)]\} \quad \text{for} \quad \xi < \xi_- .$$

(3.15)

The velocity potential fluctuation in the far upstream and far downstream regions depends upon the acoustic excitation, the acoustic response of the cascade and, in the far

8

downstream region, the vortical fluctuation associated with the rotational velocity and the vorticity shed at the blade trailing edges and convected along the blade wakes. We set

$$\tilde{\phi}(\mathbf{x}, t) = \tilde{\phi}_E(x, t) + \tilde{\phi}_R(x, t) \quad \text{for } \xi \lessgtr \xi_{\mp} , \tag{3.16}$$

where ϕ_E is the potential due to the acoustic or irrotational excitation at inlet and exit, and ϕ_R is the potential associated with the acoustic response of the blade row to the imposed unsteady excitation and the far downstream vortical fluctuation. The potential component ϕ_E is a solution of (3.6), with steady flow properties set at their free-stream values, which is subject to the requirement that acoustic excitations must either attenuate as they approach the blade row or propagate and carry energy towards or along the blade row. We find that

$$\tilde{\phi}_E(\mathbf{x}, t) = Re\{\phi_{I, \mp\infty} \exp[-\chi_{\mp\infty}\xi + i(\omega t + \kappa_{\eta, \mp\infty}\eta)]\} \quad \text{for } \xi < \xi_{\mp} \tag{3.17}$$

where the $\phi_{I, \mp\infty}$ are the complex amplitudes of the potential associated with incident pressure waves, i.e.,

$$\phi_{I, \mp\infty} = \bar{\rho}_{\mp\infty}^{-1} [\chi_{\mp\infty} V_{\mp\infty} \cos \Omega_{\mp\infty} - i(\omega + \kappa_{\eta, \mp\infty} V_{\eta, \mp\infty})]^{-1} p_{I, \mp\infty} , \tag{3.18}$$

$\kappa_{\eta, \mp\infty} = G^{-1}\sigma$ and the $\chi_{\eta, \mp\infty}$ depend upon the inlet/exit free-stream conditions, the cascade blade spacing and the temporal frequency and interblade phase angle of the unsteady excitation. Analytic solutions to (3.6) for the potential component $\tilde{\phi}_R$ which satisfy the requirements that acoustic response disturbances must either attenuate with increasing axial distance from the blade row or propagate carrying energy away from or parallel to the blade row and vorticity must be convected downstream are given in Ref. [21]. These solutions contain constants, i.e., the Fourier amplitudes of the continuous acoustic and rotational velocity responses and the complex amplitudes of the discontinuities in the potential, $[\![\phi]\!]_{\text{Ref}}$, and rotational velocity, $[\![\mathbf{v}_R]\!]_{\text{Ref}}$, at a reference wake location, that are determined by matching the far field analytic solutions to near field numerical solutions.

3.2 Discussion

The foregoing linearized equations account for the effects of blade geometry, mean blade loading and transonic, including moving shock phenomena, on the unsteady fluctuations arising from small-amplitude time-dependent excitations of nonuniform isentropic and irrotational steady background flows. The unsteady equations are linear and contain variable coefficients that depend upon the underlying steady flow.

As a consequence of the Goldstein velocity splitting, the linearized unsteady equations are coupled only sequentially. Thus, the entropy fluctuation is independent of the unsteady velocity and depends, therefore, only upon the the prescribed upstream entropic disturbance. The rotational velocity fluctuation is independent of the unsteady potential and depends only upon the entropy fluctuation and the prescribed upstream rotational velocity disturbance. The unsteady potential fluctuation depends upon the entropy and rotational velocity fluctuations, the prescribed blade motion, and the prescribed upstream and downstream pressure excitations. Note that, if either a prescribed blade motion (the flutter problem) or an incident acoustic disturbance is the only source of unsteady excitation, then $\tilde{s} \equiv \tilde{\mathbf{v}}_R \equiv 0$ and

9

only a single field equation, i.e., (3.6) with right-hand-side set equal to zero, must be solved to determine the first-order unsteady flow field.

Numerical resolutions of the linearized unsteady problem are required to determine the aerodynamic response information needed for aeroelastic and aeroacoustic predictions, i.e., the unsteady pressures and global unsteady airloads acting at the blade surfaces and the unsteady pressure field. Because of the cascade geometry and the assumed form of the unsteady excitations (i.e., harmonic in t and η), the first-order or linearized unsteady flow properties must be harmonic in time, e.g.,

$$\tilde{\mathbf{v}}(\mathbf{x}, t) = Re\{\mathbf{v}(\mathbf{x})e^{i\omega t}\} . \tag{3.19}$$

In addition, they must satisfy a circumferential periodicity condition, e.g.,

$$\mathbf{v}(\mathbf{x} + m\mathbf{G}) = \mathbf{v}(\mathbf{x})e^{im\sigma} . \tag{3.20}$$

Thus, a numerical resolution of the time-independent linearized unsteady flow problem is required only over a single extended blade-passage region of the cascade. Since analytic far-field solutions have been determined, the numerical solution domain can be restricted further to a single extended blade-passage region of finite extent in the axial direction, as shown in Figure 3.

Numerical solutions for the complex amplitudes (s, $\mathbf{v}_R$ and ϕ) of the unsteady entropy, rotational velocity and velocity potential can be determined in order. Since the entropy and rotational velocity fluctuations are governed by convection equations, solutions for these quantities can be determined in terms of the prescribed upstream entropy and rotational velocity distributions. The potential is governed by an elliptic equation, and therefore, boundary condition information must be supplied on the entire boundary of the extended blade-passage solution domain, i.e., on the surfaces of the blades, the stagnation streamlines upstream and downstream (wakes) of the blade row and the far-field boundaries $\xi = \xi_\mp$.

4. Entropy and Rotational Velocity Fluctuations

As demonstrated by Goldstein [16], closed form solutions for the entropy and rotational velocity fluctuations throughout an extended blade passage region can be determined in terms of the drift (Δ) and stream (Ψ) functions of the steady background flow. The former measures the time required for a fluid particle to traverse the distance between points on a streamline. For the present application we define the drift and stream functions as follows

$$\Delta(\mathbf{x}) = \Delta(\mathbf{x}_-) + \int_{\mathbf{x}_- + \mathbf{e}_N [\Psi(\mathbf{x}) - \Psi(\mathbf{x}_-)]/(\bar{\rho}V)_{-\infty}}^{\mathbf{x}} V^{-1} d\tau_\Psi \tag{4.1}$$

and

$$\Psi(\mathbf{x}) = \Psi(\mathbf{x}_-) + \int_{\mathbf{x}_-}^{\mathbf{x}} \bar{\rho}(\mathbf{e}_z \times \mathbf{V}) \cdot d\tau , \tag{4.2}$$

In equations (4.1) and (4.2), $\mathbf{x}_-$ is the position vector to the point of intersection (ξ_-, η_-) of the reference blade stagnation streamline and the axial line $\xi = \xi_-$, $\mathbf{e}_z$ is a unit vector that points out from the page, $\mathbf{e}_N = \mathbf{e}_z \times \mathbf{V}_{-\infty}/V_{-\infty}$ is a unit vector normal to the upstream free-stream velocity, $d\tau_\Psi$ is a differential element of arc length along a streamline, and $d\tau$ is a differential vector tangent to the path of integration in (4.2). The value of Δ at a given point $\mathbf{x}$ is determined by performing the integration in (4.1) along the streamline that passes through $\mathbf{x}$, whereas $\Psi(\mathbf{x})$ is independent of the path used to evaluate the line integral in (4.2).

We introduce the vector

$$\mathbf{X} - \mathbf{V}_{-\infty}t = V_{-\infty}(\Delta - t)\mathbf{e}_T + \Psi \mathbf{e}_N/(\bar{\rho}V)_{-\infty} , \tag{4.3}$$

where the functions $\Delta - t$ and Ψ are independent material properties (or Lagrangian coordinates) of the steady background flow, and $\mathbf{e}_T = \mathbf{V}_{-\infty}/V_{-\infty}$ is a unit vector pointing in the direction of the upstream free-stream velocity. Furthermore, we choose the constants $\Delta(\mathbf{x}_-)$ and $\Psi(\mathbf{x}_-)$ so that $\mathbf{X} \to \mathbf{x}$, as $\xi \to -\infty$. It follows that any arbitrary scalar or vector function, say $\mathcal{F}$, of $(\mathbf{X} - \mathbf{V}_{-\infty}t)$ is convected without change by the steady background flow and that $\mathcal{F}$ is a function of $\mathbf{x} - \mathbf{V}_{-\infty}t$ far upstream of the blade row, i.e.,

$$\frac{\bar{D}}{Dt}\mathcal{F}(\mathbf{X} - \mathbf{V}_{-\infty}t) = 0 \quad \text{and} \quad \lim_{\xi \to -\infty} \mathcal{F}[(\mathbf{X} - \mathbf{V}_{-\infty}t)] = \mathcal{F}(\mathbf{x} - \mathbf{V}_{-\infty}t) . \tag{4.4}$$

The foregoing considerations permit us to write immediately the solution to the entropy transport equation (3.4) which satisfies the upstream condition (3.14) as

$$\tilde{s}(\mathbf{x}, t) = \tilde{s}_{-\infty}[(\mathbf{X} - \mathbf{V}_{-\infty}t)] = \text{Re}\{s_{-\infty} \exp[i\boldsymbol{\kappa}_{-\infty} \cdot (\mathbf{X} - \mathbf{V}_{-\infty}t)]\} = \text{Re}\{s(\mathbf{x}) \exp(i\omega t)\} , \tag{4.5}$$

where $s(\mathbf{x}) = s_{-\infty} \exp(i\boldsymbol{\kappa}_{-\infty} \cdot \mathbf{X})$ is the complex amplitude of the first-order entropy fluctuation, and $\omega = -\boldsymbol{\kappa}_{-\infty} \cdot \mathbf{V}_{-\infty}$ is the temporal frequency of the unsteady motion.

11

4.1 Rotational Velocity

The rotational velocity fluctuation can also be expressed in terms of the drift and stream functions of the steady background flow and, in this case, the prescribed upstream entropy and rotational velocity disturbances. For a two-dimensional, irrotational, steady background flow, the general solution for the rotational velocity is

$$\tilde{\mathbf{v}}_R = (\boldsymbol{\nabla} \otimes \mathbf{X}) \cdot \widetilde{\boldsymbol{\mathcal{A}}}(\mathbf{X} - \mathbf{V}_{-\infty}t) + \frac{\tilde{s}}{2}\boldsymbol{\nabla}\Phi , \tag{4.6}$$

where $\otimes$ denotes the tensor or dyadic product and $\widetilde{\boldsymbol{\mathcal{A}}}$ is an arbitrary vector function of $\mathbf{X} - \mathbf{V}_{-\infty}t$. This can be verified by substituting (4.6) into the transport equation (3.5) and performing the required algebra.

The particular solution for $\tilde{\mathbf{v}}_R$ that satisfies the far upstream condition (3.15) can then be obtained by setting

$$\widetilde{\boldsymbol{\mathcal{A}}}(\mathbf{X} - \mathbf{V}_{-\infty}t) = \tilde{\mathbf{v}}_{R,-\infty}(\mathbf{X} - \mathbf{V}_{-\infty}t) - \tilde{s}_{-\infty}(\mathbf{X} - \mathbf{V}_{-\infty}t)\mathbf{V}_{-\infty}/2 , \tag{4.7}$$

where $\tilde{s}_{-\infty}(\mathbf{X} - \mathbf{V}_{-\infty}t)$ is defined in (4.5) and

$$\tilde{\mathbf{v}}_{R,-\infty}(\mathbf{X} - \mathbf{V}_{-\infty}t) = Re\{\mathbf{v}_{R,-\infty} \exp[i\boldsymbol{\kappa}_{-\infty} \cdot (\mathbf{X} - \mathbf{V}_{-\infty}t)]\} . \tag{4.8}$$

After combining equations (4.5) through (4.8), we find that the rotational velocity fluctuation is given by

$$\tilde{\mathbf{v}}_R(\mathbf{x}, t) = Re\{[\boldsymbol{\nabla} \otimes \mathbf{X} \cdot \boldsymbol{\mathcal{A}}_{-\infty} + s_{-\infty}\boldsymbol{\nabla}\Phi/2]\exp[i\boldsymbol{\kappa}_{-\infty} \cdot (\mathbf{X} - \mathbf{V}_{-\infty}t)]\} = Re\{\mathbf{v}_R(\mathbf{x})\exp(i\omega t)\}, \tag{4.9}$$

where $\boldsymbol{\mathcal{A}}_{-\infty} = \mathbf{v}_{R,-\infty} - s_{-\infty}\mathbf{V}_{-\infty}/2$ and $\mathbf{v}_R(\mathbf{x})$ is the complex amplitude of the unsteady rotational velocity.

4.2 Modification to the Goldstein Velocity Splitting

At this point we have expressed the entropy and rotational velocity fluctuations in terms of the mean flow drift and stream functions. Therefore, these fluctuations and the source term, $\bar{\rho}^{-1}\boldsymbol{\nabla} \cdot (\bar{\rho}\tilde{\mathbf{v}}_R)$, that appears in the field equation for the unsteady potential (3.6) can be evaluated once the drift and stream functions, and their derivatives, are determined from the solution for the underlying steady flow. However, as pointed out by Goldstein and later by Atassi and Grzedzinski[20], if the steady background flow has leading-edge stagnation points, the rotational velocity, and hence, the irrotational velocity, $\boldsymbol{\nabla}\tilde{\phi}$ [c.f. (3.7) and (3.8)], will be singular along blade and wake surfaces. Such behavior is a consequence of the singular behavior of the drift function, i.e., $\Delta \rightarrow a_0 \ln n$ as $n \rightarrow 0$, where n is the normal distance from a blade or wake surface and a_0 is a constant which describes the behavior of the flow in the vicinity of a stagnation point.

Although the physical velocity $\tilde{\mathbf{v}} = \tilde{\mathbf{v}}_R + \boldsymbol{\nabla}\tilde{\phi}$ must be regular, singularities in the component velocities $\tilde{\mathbf{v}}_R$ and $\boldsymbol{\nabla}\tilde{\phi}$ impose serious difficulties on the numerical field methods needed to predict the unsteady potential. Therefore, Atassi and Grzedzinski proposed the following

12

velocity decomposition to eliminate the singular behavior from the rotational and irrotational component velocities:

$$\tilde{\mathbf{v}} = \left(\tilde{\mathbf{v}}_R + \boldsymbol{\nabla}\tilde{\phi}^*\right) + \left(\boldsymbol{\nabla}\tilde{\phi} - \boldsymbol{\nabla}\tilde{\phi}^*\right) = \tilde{\mathbf{v}}_R' + \boldsymbol{\nabla}\tilde{\phi}' , \tag{4.10}$$

where $\tilde{\phi}^*$ is a pressure-less or convected potential, i.e., $\bar{D}\tilde{\phi}^*/Dt = 0$. The rotational velocity $\tilde{\mathbf{v}}_R'$ satisfies the same transport equation, i.e., (3.5), as $\tilde{\mathbf{v}}_R$, and the velocity potential $\tilde{\phi}'$ satisfies the same field equation, (3.6), as $\tilde{\phi}$. Furthermore, if one chooses $\tilde{\phi}^*$ carefully, $\tilde{\mathbf{v}}_R'$ will be regular on blade and wake surfaces. In particular, if we set

$$\tilde{\phi}^* = \mathrm{Re}\left\{\left[-i\omega^{-1}\boldsymbol{\mathcal{A}}_{-\infty} \cdot \mathbf{V}_{-\infty} + F(\Psi)\right] \exp[i\boldsymbol{\kappa}_{-\infty} \cdot (\mathbf{X} - \mathbf{V}_{-\infty}t)]\right\} , \tag{4.11}$$

the rotational velocity, $\tilde{\mathbf{v}}_R'$, is given by

$$
\begin{aligned}
\tilde{\mathbf{v}}_R' &= Re\left\{\left[\boldsymbol{\nabla}\otimes\mathbf{X}\cdot i\boldsymbol{\kappa}_{-\infty}F + \left(c_2 + \frac{\partial F}{\partial\Psi}\right)\boldsymbol{\nabla}\Psi + s_{-\infty}\boldsymbol{\nabla}\Phi/2\right]\exp[i\boldsymbol{\kappa}_{-\infty}\cdot(\mathbf{X}-\mathbf{V}_{-\infty}t)]\right\} \\
&= Re\{\mathbf{v}_R'(\mathbf{x})\exp(i\omega t)\} ,
\end{aligned}
\tag{4.12}
$$

where $c_2 = -(\bar{\rho}_{-\infty}\omega)^{-1}(\boldsymbol{\kappa}_{-\infty} \times \boldsymbol{\mathcal{A}}_{-\infty}) \cdot \mathbf{e}_z$. $F(\Psi)$ is a complex function that depends upon, among other things, the behavior of the mean flow in the vicinity of a stagnation point. It can be chosen in such a way that the rotational velocity vanishes on blade and wake surfaces. In particular, for two-dimensional cascade flows Atassi and Grzedzinski set

$$F(\Psi) = \frac{(\boldsymbol{\kappa}_{-\infty} \times \boldsymbol{\mathcal{A}}_{-\infty}) \cdot \mathbf{e}_z G \cos\Omega_{-\infty}}{2\pi(\omega/V_{-\infty})(1 - ia_0\omega)} \sin\left[\frac{2\pi[\Psi(\mathbf{x}) - \Psi(\mathbf{x}_-)]}{G(\bar{\rho}V)_{-\infty}\cos\Omega_{-\infty}}\right] \tag{4.13}$$

This choice of F eliminates the singular behavior of the rotational velocity. Indeed, $\tilde{\mathbf{v}}_R' \equiv 0$ on blade and wake surfaces. However, the potential equation source term, $\bar{\rho}^{-1}\boldsymbol{\nabla} \cdot (\bar{\rho}\tilde{\mathbf{v}}_R')$, is still singular at these surfaces.

Equations (4.5) and (4.12) relate the complex amplitudes of the first-order unsteady entropy (s) and rotational velocity ($\mathbf{v}_R'$) fluctuations to the prescribed amplitudes, $s_{-\infty}$ and $\mathbf{v}_{R,-\infty}$, and wave number, $\boldsymbol{\kappa}_{-\infty}$, at inlet, and to the velocity, drift function and stream function of the steady background flow. Note that $\mathbf{v}_R'$ depends upon Δ and Ψ and the first partial derivative of these functions. Therefore, the unsteady vorticity, $\boldsymbol{\zeta} = \boldsymbol{\nabla} \times \mathbf{v}_R'$, and the source term that appears in the potential equation for ϕ', i.e., $\bar{\rho}^{-1}(\boldsymbol{\nabla} \cdot (\bar{\rho}\mathbf{v}_R'))$, depend also upon the second partial derivatives of the mean flow drift and stream functions. Thus, an accurate solution for the nonlinear steady background flow is a critical prerequisite to properly determining the unsteady effects associated with inlet entropic and vortical excitations.

4.3 Boundary-Value Problem for the Modified Potential

The complex amplitude of the unsteady potential (ϕ') is determined as a solution of the field equation

$$\frac{\bar{D}_\omega}{Dt}\left(A^{-2}\frac{\bar{D}_\omega\phi'}{Dt}\right) - \bar{\rho}^{-1}\boldsymbol{\nabla} \cdot (\bar{\rho}\boldsymbol{\nabla}\phi') = \bar{\rho}^{-1}\boldsymbol{\nabla} \cdot (\bar{\rho}\mathbf{v}_R') . \tag{4.14}$$

13

This solution is subject to the following surface conditions:

$$\boldsymbol{\nabla}\phi' \cdot \mathbf{n} = [\bar{D}_\omega \mathbf{r}/Dt - (\mathbf{r}\cdot\boldsymbol{\nabla})\boldsymbol{\nabla}\Phi]\cdot\mathbf{n}\ , \quad \mathbf{x}\in B_m\ ; \tag{4.15}$$

$$\frac{[\![\bar{D}_\omega\phi']\!]}{Dt} = 0 \quad \text{and} \quad [\![\boldsymbol{\nabla}\phi']\!]\cdot\mathbf{n} = 0\ , \quad \mathbf{x}\in W_m\ ; \tag{4.16}$$

and

$$[\![\bar{\rho}(\boldsymbol{\nabla}\phi' - A^{-2}\frac{\bar{D}_\omega\phi}{Dt}\boldsymbol{\nabla}\Phi)]\!]\cdot\mathbf{n} + [\![\bar{\rho}]\!]\mathbf{v}'_R\cdot\mathbf{n} = [\![\bar{\rho}]\!][i\omega t + (\boldsymbol{\nabla}\Phi\cdot\boldsymbol{\tau})\boldsymbol{\tau}\cdot\boldsymbol{\nabla}](\mathbf{r}\cdot\mathbf{n})$$

$$+\ (\mathbf{r}\cdot\mathbf{n})\boldsymbol{\tau}\cdot\boldsymbol{\nabla}([\![\bar{\rho}]\!]\boldsymbol{\nabla}\Phi\cdot\boldsymbol{\tau}) \text{ and } [\![\phi']\!] = -\mathbf{r}\cdot\mathbf{n}[\![\boldsymbol{\nabla}\Phi]\!]\cdot\mathbf{n}\ , \quad \mathbf{x}\in \mathrm{Sh}_{m,n}\ . \tag{4.17}$$

Equations (4.14)–(4.17) are obtained after substituting (4.10) into (3.6)–(3.11), and replacing $\tilde{\phi}'$ by $\phi'\exp(i\omega t)$, $\mathcal{R}$ by $\mathbf{r}\exp(i\omega t)$ and $\bar{D}/Dt$ by $\bar{D}_\omega/Dt = i\omega + \boldsymbol{\nabla}\Phi\cdot\boldsymbol{\nabla}$. Finally, analytical solutions are available [21] to describe the behavior of ϕ' far from the blade row. These can be matched to near-field numerical solutions and, therefore, serve to complete the specification of the time-independent boundary-value problem for ϕ'.

At this point, we have presented a relatively complete linearized unsteady aerodynamic formulation to describe general (i.e., entropic, vortical and acoustic) perturbations of subsonic and discontinuous transonic mean flows. Numerical methods for predicting the unsteady aerodynamic response of subsonic and transonic cascades to structural and acoustic excitations have been reported in Refs. [18, 19 and 21]. Methods for predicting cascade response to entropic and vortical excitations are described in the following section of this report. At present, the numerical solution procedures for the entropic and vortical gust problems have only been developed and implemented for subsonic flows. The development of such procedures for the transonic gust response problem remains, therefore, as a subject for future work.

5. Numerical Solution Procedures

The theoretical foundation for the linearized unsteady aerodynamic analysis has been established. We will proceed to discuss the procedures used to evaluate the complex amplitudes of the unsteady entropy (s), rotational velocity $(\mathbf{v}'_R)$, and source term $[\bar{\rho}^{-1}\boldsymbol{\nabla}\cdot(\bar{\rho}\mathbf{v}'_R)]$ throughout an extended blade-passage solution domain. The finite-difference numerical model used to solve the boundary-value problem for the complex amplitude (ϕ') of the unsteady potential has been described in previous work. Since the only changes to this model required for the entropic and vortical gust problems are those needed to accomodate the source term in the field equation (4.14) and rotational velocity effects in the analytical far-field solutions for the unsteady potential [21], we will not repeat the description here, but simply refer the reader to Refs. [11, 18 and 19] for the details.

5.1 Generation of the Streamline Grid

In section 4, it was shown that the unsteady entropy and rotational velocity can be expressed in terms of the drift and stream functions, Δ and Ψ, of the steady background flow. For this reason it is convenient to use an H-grid in which one set of mesh lines are the streamlines of the steady background flow for the numerical evaluation of these unsteady flow variables. The first step in the grid generation process is to specify the grid point locations on the boundary of the physical solution domain, i.e., a single extended blade-passage region of finite extent as shown in Figure 3. The boundaries of this region are the upper and lower surfaces of the blades, the upstream and downstream axial lines $\xi = \xi_{\mp}$ and the upstream and downstream mean-flow stagnation streamlines. The stagnation streamline locations are determined from the solution for the nonlinear steady background flow.

The locations of the stagnation streamlines are found by particle tracing, i.e., by integrating the equation

$$\frac{\partial \mathbf{x}}{\partial \tau} = \mathbf{V} \, , \tag{5.1}$$

using a variable-step, fifth-order, Runge-Kutta algorithm [24], from the leading and trailing edges of a blade to the far upstream $(\xi = \xi_-)$ and far downstream $(\xi = \xi_+)$ boundaries. The location of the leading-edge stagnation point is determined by curve fitting the blade profile and the steady potential distribution along the blade using cubic splines. The stagnation point is defined as the point on this curve at which the steady potential has a minimum value, and is found by bisection. After integrating equation (5.1) from the leading-edge stagnation and the trailing-edge points to the far-field boundaries, the calculated points on the stagnation streamlines are curve fit using cubic splines.

Once the boundaries of the H-grid have been determined, the locations of the interior points are found using an elliptic grid generation technique similar to that developed by Thompson et al. [25]. An elliptic grid generator offers the advantages that relatively smooth grids can be determined, and grids for complicated flow geometries, such as those associated with cascades of thick, highly cambered blades, are easy to generate. Following Thompson et al., the grid lines are described by the partial differential equations

$$\boldsymbol{\nabla}^2\Xi = \mathcal{P} \tag{5.2}$$

and

$$\nabla^2 \mathcal{H} = \mathcal{Q} \,. \tag{5.3}$$

The "axial" and "streamwise" grid lines correspond to lines of constant Ξ and $\mathcal{H}$, respectively. The functions $\mathcal{P}$ and $\mathcal{Q}$ can be used to control the spacing and orthogonality of the grid lines. In this investigation, however, we have chosen the function $\mathcal{Q}$ so that $\mathcal{H}$ is the stream function Ψ of the irrotational steady background flow, i.e., we set $\mathcal{Q} = \mathbf{V} \times \boldsymbol{\nabla}\bar{\rho}$.

Rather than solve equations (5.2) and (5.3) for Ξ and Ψ as functions of ξ and η, we invert these equations to determine ξ and η as functions of Ξ and Ψ. It can be shown that

$$\alpha\frac{\partial^2\xi}{\partial\Xi^2} - 2\beta\frac{\partial^2\xi}{\partial\Xi\partial\Psi} + \gamma\frac{\partial^2\xi}{\partial\Psi^2} = -D^2\left(\mathcal{P}\frac{\partial\xi}{\partial\Xi} + \mathcal{Q}\frac{\partial\xi}{\partial\Psi}\right) \tag{5.4}$$

and

$$\alpha\frac{\partial^2\eta}{\partial\Xi^2} - 2\beta\frac{\partial^2\eta}{\partial\Xi\partial\Psi} + \gamma\frac{\partial^2\eta}{\partial\Psi^2} = -D^2\left(\mathcal{P}\frac{\partial\eta}{\partial\Xi} + \mathcal{Q}\frac{\partial\eta}{\partial\Psi}\right) \,, \tag{5.5}$$

where D is the determinant of the Jacobian of the independent variable transformation, $(\Xi, \Psi) \to (\xi, \eta)$, i.e.,

$$D = \frac{\partial\xi}{\partial\Xi}\frac{\partial\eta}{\partial\Psi} - \frac{\partial\xi}{\partial\Psi}\frac{\partial\eta}{\partial\Xi} \,, \tag{5.6}$$

and the coefficients α, β, and δ are given by

$$\alpha = \left(\frac{\partial\xi}{\partial\Psi}\right)^2 + \left(\frac{\partial\eta}{\partial\Psi}\right)^2, \quad \beta = \frac{\partial\xi}{\partial\Xi}\frac{\partial\xi}{\partial\Psi} + \frac{\partial\eta}{\partial\Xi}\frac{\partial\eta}{\partial\Psi}, \quad \delta = \left(\frac{\partial\xi}{\partial\Xi}\right)^2 + \left(\frac{\partial\eta}{\partial\Xi}\right)^2 \tag{5.7}$$

The nonlinear partial differential equations (5.4) and (5.5) are solved numerically over a rectangular region in Ξ, Ψ-space, subject to Dirichlet conditions on ξ and η at the boundary. The values of ξ and η along the boundary of the rectangular domain are defined by their values at the prescribed points along the boundary of the extended blade-passage physical domain. Because the Ξ, Ψ-grid is rectangular, difference approximations are easy to construct. For example, if the spacings between the grid lines are constant (i.e., $\Delta\Xi_i = \Delta\Xi$, $\Delta\Psi_j = \Delta\Psi$), then the difference equation for the ξ-coordinate at the i, jth node has the form

$$\frac{\alpha_{i,j}}{\Delta\Xi^2}(\xi_{i+1,j} - 2\xi_{i,j} + \xi_{i-1,j}) - \frac{1}{2}\frac{\beta_{i,j}}{\Delta\Xi\Delta\Psi}(\xi_{i+1,j+1} - \xi_{i+1,j-1} - \xi_{i-1,j+1} + \xi_{i-1,j-1})$$

$$+ \frac{\gamma_{i,j}}{\Delta\Psi^2}(\xi_{i,j+1} - 2\xi_{i,j} + \xi_{i,j-1}) = -D_{i,j}^2\left(\mathcal{P}_{i,j}\left(\frac{\partial\xi}{\partial\Xi}\right)_{i,j} + \mathcal{Q}_{i,j}\left(\frac{\partial\xi}{\partial\Psi}\right)_{i,j}\right) \tag{5.8}$$

A similar equation describes the η-coordinate at the i, jth node. In equation (5.8), it is assumed that the transformed grid spacings, $\Delta\Xi_i$ and $\Delta\Psi_j$, are constant. In the present investigation, however, nonconstant transformed grid spacings are used to control the spacings in the physical plane. For example, by choosing appropriate values of $\Delta\Xi_i$ and $\Delta\Psi_j$, the streamwise and axial grid lines can be packed near blade and wake surfaces and near the leading and trailing edges of the blades, respectively.

16

The difference equations for ξ and η are solved using a successive line over-relaxation procedure in which the coefficients α, β and δ, and the terms on the right-hand-sides of (5.4) and (5.5) are lagged, i.e., they are computed just prior to each line over-relaxation. Also, because the function $\mathcal{Q}$ is fairly expensive to compute, and because it is fairly insensitive to small changes in ξ and η, this function is updated only every tenth iteration.

A typical grid generated for a compressor cascade operating at an inlet Mach number of 0.3 and an inlet flow angle of 40.0 deg is shown in Figure 3. The blades are thick and highly cambered, and the cascade has a gap-to-chord ratio, G, of 0.6 and a stagger angle Θ of 15 deg. The steady flow, which was determined using the analysis of Ref. [22], is used to generate the stagnation streamlines and to determine the function $\mathcal{Q}$ in (5.4) and (5.5). For the grid shown in Figure 3, the function $\mathcal{P}$ was set equal to zero. Note the clustering of streamlines near the blade and wake surfaces and axial lines in the vicinity of the blade leading and trailing edges, which is achieved by employing nonconstant rectangular grid spacings, $\Delta\Xi_i$ and $\Delta\Psi_j$, in the transformed plane.

5.2 Evaluation of the Drift Function

Because a streamline mesh is used, the drift function can be evaluated by straightforward numerical integrations of equation (4.1). The procedure is simply to specify the drift function along the far upstream boundary $\xi = \xi_-$, and then to evaluate this function along each streamline using the second-order difference approximation

$$\Delta_{i+1,j} = \Delta_{i,j} + \frac{\tau_{i+1,j} - \tau_{i,j}}{0.5\left(|\mathbf{V}_{i+1,j}| + |\mathbf{V}_{i,j}|\right)} \tag{5.9}$$

Since the steady flow speed, V, appears in the denominator of the integrand in equation (4.1), the drift function will be singular at flow stagnation points. Hence, for a blade having a blunt leading edge this function will be singular along the entire surface of each blade and its wake.

The calculated drift and stream function contours for the the compressor cascade of Figure 3 are shown in Figure 4. Note that, because of the manner in which the drift function has been defined in (4.1), the drift function contours are orthogonal to the streamlines far upstream of the blade row. This is not a requirement, but it does simplify the analytical expressions (4.5) and (4.12) for the entropy and rotational velocity. Note also the singular behavior near the blade and wake surfaces indicated by the drift function contours.

The derivatives of the drift and stream functions at a given grid point are determined using the finite difference operators developed by Caspar and Verdon [18]. Because the drift function is singular at blade and wake surfaces, one-sided difference approximations are used to evaluate its derivatives at points on the first streamlines removed from these surfaces. The derivatives of the drift function at the blade and wake surfaces are singular, but are not required to evaluate $\mathbf{v}'_R$ and $\bar{\rho}^{-1}\boldsymbol{\nabla} \cdot (\bar{\rho}\mathbf{v}'_R)$ at field points.

As noted previously, a numerical resolution of the linear, variable-coefficient, unsteady, boundary-value problem that governs the velocity potential is required over a single extended blade-passage region of finite extent. The field equation (4.14) must be solved in continuous regions of the flow, subject to the boundary or jump conditions that are imposed at the mean positions of the blade, wake and shock surfaces. Also, the unsteady near-field numerical solution must be matched to far-field analytical solutions (see [21]) at finite axial distances

17

(i.e., at $\xi = \xi_{\mp}$) upstream and downstream from the blade row. The numerical procedures for determining ϕ' are described in Refs. [11, 18 and 19].

6. Numerical Results

Unsteady aerodynamic response predictions are given below to demonstrate important features of the foregoing linearized analysis. The unsteady flows considered here are entirely subsonic. Steady background flows have been determined using the methods of Ref. [22]. In each case a Kutta condition has been applied at blade trailing edges and therefore, only inlet uniform flow information, e.g., $M_{-\infty}$ and $\Omega_{-\infty}$, must be specified for the steady calculation. First-harmonic unsteady solutions were determined on an H-type mesh (see Figure 3) consisting of 120 "axial" lines and 30 mean-flow streamlines. These were packed near the blade and wake surfaces and near the blade edges, respectively.

For the most part we have considered cascades consisting of blades that are constructed by superposing the thickness distribution of a modified NACA four-digit series airfoil, i.e.,

$$T(x) = H_T[2.969x^{1/2} - 1.26x - 3.516x^2 + 2.843x^3 - 1.036x^4], \qquad 0 \le x \le 1 , \qquad (6.1)$$

on a circular-arc camber line. Here, H_T is the nominal blade thickness, and the coefficient of the x^4 term in (6.1) differs from that used in the standard NACA airfoil definition [26], i.e., -1.015, so that the example blades close in wedge-shaped trailing edges. The camber distribution is given by

$$C(x) = H_C - R + [R^2 - (x - 0.5)^2]^{1/2} , \qquad 0 \le x \le 1 , \qquad (6.2)$$

where H_C (> 0) is the height of the circular-arc camber line at blade midchord and $R = (2H_C)^{-1}(0.25 + H_C^2)$ is the radius of this camber line. Thus, the surface coordinates of the reference blade are given by

$$[X,Y]_{\mathrm{B}}^{\pm} = [x \mp 0.5T(x)\sin\theta, \; C(x) \pm 0.5T(x)\cos\theta] , \qquad 0 \le x \le 1 , \qquad (6.3)$$

where $\theta = \tan^{-1}(dC/dx)$, and the superscripts $+$ and $-$ refer to the upper and lower surfaces of the blade.

We will first apply the present analysis to flat-plate, $H_T = 0$ and $H_C = 0$, cascades in which the blade mean positions are aligned with the inlet free-stream flow direction, i.e., $\Theta = \Omega_{-\infty}$, and compare present response predictions with those based on Smith's [4] classical linearized analysis. We will then consider cascades of uncambered NACA airfoils and cascades of cambered, 6% thick NACA airfoils to study the effects of blade thickness and mean loading on the unsteady aerodynamic response at a blade surface to an incident vortical gust. Finally, we will examine the response of three more realistic configurations: a compressor exit guide vane (EGV) consisting of thick, highly cambered blades ($H_T = 0.12$, $H_C = 0.13$), a high speed compressor cascade consisting of moderately thick and cambered ($H_T = 0.06$ and $H_C = 0.05$) blades, and a turbine cascade. As a representative turbine configuration we have selected the fourth standard configuration of Ref. [27]. However, we have extended the blade profiles defined in [27] so that our example turbine blades also close in wedge-shaped trailing edges.

We are primarily interested in the linearized unsteady flows excited by vortical gusts, such as those that arise, for example, from wakes off the blades of an adjacent upstream blade row. If the "circumferential" spacing between the blades in the adjacent upstream row is G_{EXC}

and if these blades move at velocity $V_{\text{EXC}}\mathbf{e}_\eta$ relative to the blade row under consideration, then the interblade phase angle and temporal frequency of the fundamental or blade passing vortical excitation are $\sigma = \kappa_{\eta,-\infty}G = -2\pi G/G_{\text{EXC}}$ and $\omega = -\kappa_{\eta,-\infty}V_{\text{EXC}} = \sigma G^{-1}V_{\text{EXC}}$, where $\kappa_{\eta,-\infty} = -2\pi/G_{\text{EXC}}$ is the circumferential wave number of this excitation. For the present study, we will choose $\sigma = -2\pi$, $\omega = 5$ and $v_g = (1,0)$ to describe a "standard" vortical gust excitation. Here, v_g is the complex amplitude of the gust velocity component normal to the inlet free-stream flow direction at the point $(x,y) = (0,0)$. In particular, v_g is the amplitude at the leading edge of the reference blade that would exist if the incident gust was convected through the blade row, without distortion, by the uniform inlet flow.

6.1 Flat-Plate Cascade

The example flat-plate cascade has a stagger angle (Θ) of 45 deg and a blade spacing (G) of 1.0 and operates at three different inlet Mach numbers, i.e., $M_{-\infty} = 0.3$, 0.5 and 0.7. In each case the inlet flow angle $(\Omega_{-\infty})$ is 45 deg and vortical excitations with $v_g = (1,0)$ and $\omega = 5$ are imposed far upstream of the blade row. Since the inlet free-stream flow direction is aligned with the blade mean positions, the local steady Mach number, $M(= M_{-\infty})$, and flow angle, $\Omega(= \Omega_{-\infty})$, are constants for the flat-plate flow fields. Predicted unsteady pressure-difference distributions, $\Delta p(x) = p[x, y_{\text{B}}^-(x)] - p[x, y_{\text{B}}^+(x)]$, acting on the reference $(m = 0)$ blade for the standard vortical excitation at $\sigma = -2\pi$ (-360 deg) are shown in Figure 5, where the solid and dashed curves represent the results of the present and of Smith's analysis, respectively. Recall that in the present analysis the unsteady potential (4.14) equation contains the source term $\bar{\rho}^{-1}\boldsymbol{\nabla} \cdot (\bar{\rho}\mathbf{v}_R')$ and $\boldsymbol{\nabla}\phi' \cdot \mathbf{n} = 0$ on blade surfaces, whereas in the classical linearization the potential equation is homogeneous, and the normal component of the irrotational velocity must cancel the normal component of the gust velocity at blade surfaces. The results in Figure 5 show that the two analyses yield pressure-difference predictions that are in very good agreement for $M_{-\infty} = 0.3$ and $M_{-\infty} = 0.5$, but the agreement is not quite so satisfactory for $M_{-\infty} = 0.7$.

Similar results for unsteady flows driven by a prescribed blade translations, i.e., $\mathcal{R} = h_y \exp(i\omega t)\mathbf{e}_y$, normal to the mean positions of the blade chords are shown in Figure 6 for an excitation with $h_y = (1,0)$, $\omega = 5$ and $\sigma = -2\pi$. The unsteady flows are irrotational and therefore, the unsteady potential equation is homogeneous. The agreement between the pressure-difference predictions obtained from the present numerical analysis and Smith's semi-analytical solution procedure is somewhat better than that for the vortical excitation, but discrepancies still exist at the highest inlet Mach number. We suspect that the differences between the present and Smith's solutions for $M_{-\infty} = 0.7$ occur because the computational grid used in the numerical calculation was not dense enough to resolve the high wave number acoustic response phenomena that are associated with high subsonic Mach numbers and high excitation frequencies. Therefore, such differences should disappear if a mesh of sufficient density is employed in the numerical calculation.

The unsteady lift, f_y, responses at the reference blade of the flat-plate cascade operating at $M_{-\infty} = 0.5$ to prescribed vortical excitations with $v_g = (1,0)$ and $\omega = 5$ and to prescribed blade translations with $h_y = (1,0)$ and $\omega = 5$ are plotted versus interblade phase angle in Figure 7. The excitations occur over interblade phase range extending from -3π (-540 deg) to $-\pi$ (-180 deg). Abrupt changes in the lift response curves occur at $\sigma = -473.8$ deg

and -471.1 deg. The excitations at these phase angles produce resonant acoustic response disturbances in the far field. The lift responses to the vortical excitations as predicted by the numerical and semi-analytical solution procedures are in good agreement; however, this agreement is not nearly as good as that between the lift responses to the blade translational excitations, suggesting that the present numerical analysis still requires some improvements so that the source term, $\bar{\rho}^{-1}\nabla \cdot (\bar{\rho}\mathbf{v}'_R)$, can be evaluated more accurately.

6.2 Effects of Blade Thickness and Mean Loading

We proceed to evaluate the present analysis by applying it to two families of cascade configurations. For the first, $\Theta = 45$ deg, $G = 1$, the blades are uncambered ($H_C = 0$), but the blade thickness varies from $H_T = 0$ to $H_T = 0.12$; for the second, the blade spacing, $G = 1$, and thickness, $H_T = 0.06$, are constant, but the height of the circular-arc blade camber line and the cascade stagger angle vary in such a manner that the tangents to the camber lines at the blade leading edges are aligned with the inlet free-stream flow direction, i.e., $\Theta = \Omega_{-\infty} - \theta$. The cascades in the first family operate at an inlet Mach number of 0.3 and an inlet flow angle of 45 deg; those in the second family, at an inlet Mach number of 0.5 and an inlet flow angle of 45 deg. The cascades in both families are subjected to the standard vortical gust excitation at $v_g = (1,0)$, $\omega = 5$ and $\sigma = -2\pi$.

The cascades in the first family have been studied to indicate the effects of blade thickness on the unsteady aerodynamic response to a vortical gust excitation. It should be noted that although the blades are uncambered and their chord lines are aligned with the inlet flow direction, i.e., $\Theta = \Omega_{-\infty}$, there is a small mean or steady lift force acting on the blades of these cascades for $H_T \neq 0$. This force increases in magnitude, from 0 for $H_T = 0$ to 0.062 for $H_T = 0.12$, with increasing blade thickness. The exit Mach numbers ($M_{+\infty}$) vary from 0.3 for $H_T = 0$ to 0.314 for $H_T = 0.12$, and the exit flow angles ($\Omega_{+\infty}$), from $45°$ to $47.22°$. The unsteady pressure-difference distributions along the reference blades of the cascades with $H_T = 0, 0.04, 0.08$ and 0.12 are shown in Figure 8. These results indicate that blade thickness has only a limited impact on the unsteady aerodynamic response to a vortical excitation. Indeed, the pressure-difference response for the cascade of 2% thick blades (not shown) closely resembles that for the flat-plate ($H_T = 0$) cascade. This result provides an important check on the present analysis, indicating that the mathematical difficulties associated with mean flow stagnation at blade leading edges have been successfully overcome.

The second cascade family, described above, has been studied to indicate the effects of blade loading on the response of cascades to incident vortical gusts. Numerical calculations were performed for cascades consisting of 6% thick blades with $H_C = 0, 0.04, 0.08$ and 0.12. The cascade stagger angles corresponding to these values of H_C are $\Theta = 45$ deg, 36 deg, 28.4 deg and 22.6 deg, respectively. The calculated exit Mach numbers and flow angles are 0.515, 0.395, 0.346 and 0.328 and 46.2 deg, 31.9 deg, 18.6 deg and 6.9 deg, respectively. The predicted values for the steady lift force acting on each blade are -0.036 for $H_C = 0.$, 0.260 for $H_C = 0.04$, 0.412 for $H_C = 0.08$, and 0.508 for $H_C = 0.12$. The steady Mach number distributions along the blade surfaces are shown in Figure 9; the unsteady pressure-difference responses to the standard vortical excitation, in Figure 10. The latter indicate that the effect of mean blade loading, or mean flow turning, on the unsteady aerodynamic response of cascades to incident vortical excitations can be significant.

21

6.3 Compressor and Turbine Cascades

We turn now to more realistic cascade configurations — a compressor exit guide vane (EGV), a high-speed compressor cascade, and a turbine cascade. In each case we will compare the unsteady response of the actual cascade to a corresponding flat-plate cascade having the same blade spacing and operating at the same inlet flow conditions. However, the flat-plate blades are staggered so that their mean positions are aligned with the mean inlet flow direction, i.e., $\Theta = \Omega_{-\infty}$. Thus, the local steady Mach number, $M = M_{-\infty}$, and flow angle $\Omega = \Omega_{-\infty}$, are constants for the flat-plate configurations. For each cascade we will examine the behavior of the unsteady vorticity, source term and pressure throughout an extended blade passage region. The source term is presented for its mathematical rather than its physical significance. This term depends upon the manner in which the imposed vortical gust is convected by the mean flow. An accurate numerical description of the source term is crucial to the successful prediction of the unsteady pressure field excited by the gust interaction. We will also examine the reference-blade pressure-difference responses that result from the interaction between each blade row and the standard vortical excitation at $v_g = (1,0)$, $\omega = 5$ and $\sigma = -2\pi$, and the unsteady lift responses to vortical excitations at $v_g = (1,0)$, $\omega = 5$ and $-3\pi \leq \sigma \leq -\pi$.

Exit Vane Guide

The compressor exit guide vane (EGV) consists of thick, $H_T = 0.12$, highly cambered, $H_C = 0.13$, modified NACA airfoils. It has a stagger angle of 15 deg, a blade spacing of 0.6 and operates at a prescribed inlet Mach number and inlet flow angle of 0.3 and 40 deg, respectively. The calculated exit Mach number, exit flow angle and mean lift force acting on each blade are 0.226, -7.4 deg and 0.36, respectively. The steady Mach number contours and Mach number distributions along a blade surface for this configuration are depicted in Figure 11.

We will examine the unsteady response of the EGV cascade to incident vortical excitations and compare it to that for the corresponding flat-plate cascade with $\Theta = \Omega = 40$ deg, $G = 0.6$ and $M = 0.3$. Contours of the real part of the complex amplitude of the unsteady vorticity, source term and pressure for the EGV and flat-plate cascades are shown in Figures 12, 13 and 14, respectively, for the standard vortical gust excitation. The prescribed gust is severely distorted as it is convected by the nonuniform mean flow through the EGV blade row. In contrast, it is convected without distortion by the uniform mean flow through the flat-plate blade row. Also, since the vorticity is convected at different mean velocities along the upper and lower surfaces of the EGV blades, it is discontinuous across their wakes. The contours shown in Figure 13 illustrate the rather strong variations in the source term, $\bar{\rho}^{-1}\boldsymbol{\nabla} \cdot \bar{\rho}\mathbf{v}'_R$, particularly for the EGV configuration, that can occur within an extended blade passage solution domain. Finally, the pressure contours depicted in Figure 14 indicate that the unsteady pressure behaviors associated with the EGV and flat-plate cascades are similar far upstream, but differ substantially in the vicinity of the blade surfaces and downstream of the blade row.

The pressure-difference responses along the reference blade of the EGV and flat-plate cascades to the standard vortical excitation at $v_g = (1,0)$, $\omega = 5$ and $\sigma = -2\pi$ are shown in Figure 15. The unsteady lift forces acting on the reference blades of the two cascades

are plotted versus interblade phase angle for vortical excitations at $v_g = (1, 0)$, $\omega = 5$ and $-3\pi \leq \sigma \leq -\pi$ in Figure 16. The excitations at $\sigma = -404.2$ deg and -293.9 deg produce resonant acoustic response disturbances far upstream and far downstream of the flat-plate cascade and far upstream of the EGV; those at $\sigma = -414.3$ deg and -308.8 deg produce such response disturbances far downstream of the EGV. The results in Figures 15 and 16 indicate the relative importance of nonuniform mean flow phenomena on the local and global unsteady aerodynamic response at a blade surface for cascades subjected to incident vortical excitations. It should be noted that the unsteady lift acts in the direction of the positive y-axis (see Figure 1), and this is inclined at different angles relative to the axial flow direction for the EGV ($\Theta = 15$ deg) and flat-plate ($\Theta = 40$ deg) cascades. Also, the the flat-plate lift distributions in Figure 16 are in good agreement with Smith's results, except for interblade phase angles lying in the range $-540 \deg < \sigma < -404.2 \deg$, where the out-of-phase, i.e, $Im\{f_y\}$, lift responses predicted by the two analyses are similar qualitatively but show small quantitative differences.

Compressor Cascade

The high-speed compressor cascade consists of cambered, with $H_C = 0.05$, modified NACA 0006 airfoils (i.e., $H_T = 0.06$). This cascade and the corresponding flat-plate cascade operate at high-subsonic inlet conditions, i.e., $M_{-\infty} = 0.7$ and $\Omega_{-\infty} = 55$ deg, and have a gap-chord ratio, G, of unity. The NACA 0006 cascade has a stagger angle of 45 deg. The flat-plate blades are aligned with the inlet free-stream flow direction and are therefore staggered at an angle of 55 deg. The exit Mach number and flow angle for the NACA 0006 cascade are 0.446 and 40.17 deg, and the mean lift acting on each blade is 0.348. The steady Mach number contours and Mach number distributions over a blade surface for the NACA 0006 configuration are shown in Figure 17.

Unsteady flow predictions similar to those given in Figures 12–15 are presented in Figures 18–21 for the standard vortical gust. The unsteady lift responses to vortical gusts at $v_g = (1, 0)$, $\omega = 5$ and $-540 \deg < \sigma < -180 \deg$ are shown in Figure 22. Excitations at $\sigma = -494.6$ deg and $\sigma = -494.4$ deg produce resonant acoustic response disturbances far upstream of the NACA 0006 and flat-plate cascades and far downstream of the flat plate cascade. Excitations at $\sigma = -518.9$ deg and $\sigma = -420.6$ deg produce such response disturbances far downstream of the NACA 0006 cascade.

The vorticity and source term contours shown in Figures 18 and 19 indicate that the distortion of the vortical gust by the NACA 0006 cascade is much less severe than it is for the EGV (see Figures 12 and 13). Although the mean lift forces acting on the blades of the two cascades are nearly the same, the overall turning $|\Omega_{+\infty} - \Omega_{-\infty}|$ of the mean flow is much greater for the EGV (47.4 deg) than it is for the NACA 0006 compressor (14.8 deg). The pressure contours (Figure 20) for the NACA 0006 and flat-plate cascades also show much more similarity than those in Figure 14. Some differences between the NACA 0006 and the flat-plate pressure fields exist just upstream of the blade rows, where relatively large amplitude unsteady pressures are associated with the NACA 0006 configuration.

As shown in Figures 21 and 22, the unsteady pressure-difference responses of the NACA 0006 and flat-plate blades to the standard vortical excitation ($\sigma = -360$ deg) differ along the blade surfaces, but the unsteady lift responses to vortical excitations at $v_g = (1, 0)$,

23

$\omega = 5$ and $-540 \deg < \sigma < -180 \deg$ are very similar, except for interblade phase angles lying in the range $-540 \deg < \sigma < -490 \deg$. In the latter range, the numerical calculations for the flat-plate cascade do not agree with Smith's predictions. Because of this and the fact that the lift responses at $\sigma = -540$ deg and $\sigma = -180$ deg predicted by the numerical analysis for the flat-plate cascade are not identical, we believe that the numerical results for the NACA 0006 and the corresponding flat-plate cascades are incorrect for $-540 \deg < \sigma < -490 \deg$. Improvements to the present analysis are therefore required to permit a more accurate evaluation of the source term over a broad range of interblade phase angles.

Turbine Cascade

As a final example we consider the turbine cascade proposed as the fourth standard cascade configuration in [27] and a flat-plate cascade operating at the same inlet free-stream conditions. These cascades operate at an inlet Mach number of 0.19 and an inlet flow angle of 45 deg, and they have a blade spacing G of 0.76. The turbine cascade has a stagger angle of 56.6 deg and the flat-plate blades are staggered at $\Theta = \Omega = 45$ deg. The calculated exit Mach number and flow angle for the turbine are 0.49 and 72.0 deg, respectively, and the mean lift acting on each blade is -2.09. The turbine cascade turns the steady flow through an angle $|\Omega_{+\infty} - \Omega_{-\infty}|$ of 27 deg. The predicted steady Mach number contours and blade-surface Mach number distributions are shown in Figure 23.

Local unsteady response predictions for the turbine and flat-plate cascades subjected to the standard vortical gust excitation are shown in Figures 23 through 27, and the lift responses to incident vortical gusts with $v_g = (1, 0)$, $\omega = 5$ and $-540 \deg < \sigma < -180 \deg$, in Figure 28. Excitations at $\sigma = -396.8$ deg and $\sigma = -311.7$ deg produce resonant acoustic response disturbances far upstream of the turbine cascade and far upstream and far downstream of the flat-plate cascade. Excitations at $\sigma = -389.0$ deg and at $\sigma = -279.2$ deg produce such response disturbances far downstream of the turbine cascade.

As shown in Figure 24, the standard vortical gust is highly distorted as it is convected through the turbine blade row. In addition, the source term (Figure 25) associated with this gust has relatively large gradients within the passage and downstream of the turbine blade row. These give rise to high unsteady pressures (Figure 26) along the suction surface of the blades and downstream of the turbine blade row. As indicated by the results in Figure 25 the unsteady pressure fields associated with the turbine and the corresponding flat-plate cascades differ substantially. As a consequence, there are significant differences between the unsteady pressure-difference responses at the reference turbine and flat-plate blade surfaces for $\sigma = -2\pi$ (Figure 27), and between the unsteady lift responses over a significant range of interblade phase angles (Figure 28). The unsteady response predictions for the turbine and flat-plate cascades illustrate rather dramatically the substantial impact that mean flow turning can have on the unsteady aerodynamic response of cascades to incident vortical gusts. We should add that, for this example, the flat-plate lift response predicted by the present analysis and the Smith analysis are in good agreement over the entire range, $-3\pi \leq \sigma \leq -\pi$, of interblade phase angles considered.

7. Concluding Remarks

A linearized analysis for predicting the unsteady pressure response of a cascade of airfoils to external aerodynamic excitations has been presented. The unsteady flow is regarded as a small perturbation of a nonuniform isentropic and irrotational steady background flow. Goldstein's splitting, [16,17], along with a recent modification introduced by Atassi and Grzedzinski [20] have been used to decompose the linearized unsteady velocity into irrotational and rotational parts, leading to equations for the linearized unsteady entropy, rotational velocity, and velocity potential that are coupled only sequentially. The entropic and rotational velocity fluctuations are described in terms of the mean-flow drift and stream functions, and the potential fluctuation is governed by an inhomogeneous convected wave equation in which the source term depends on the rotational velocity field. In this report the analytical and numerical techniques used to determine the linearized unsteady flow have been described and demonstrated through a series of numerical examples.

Numerical studies have been conducted to evaluate the capabilities of this linearized unsteady aerodynamic analysis and the LINFLO computer code for predicting the response of cascades to incident vortical gusts. For this purpose we have considered the following configurations: flat-plate cascades, cascades of uncambered NACA 00XX airfoils, cascades of cambered NACA 0006 airfoils, a cascade of thick, highly cambered blades that is representative of the exit guide vane (EGV) of a high-pressure compressor, a high-speed compressor cascade consisting of cambered NACA 0006 blades, and a turbine cascade. In each case we have taken as a standard gust a unit-amplitude vortical excitation at reduced frequency $\omega = 5$ and interblade phase angle $\sigma - 2\pi$.

The results obtained using the present analysis were found to be in very good agreement with the results of Smith's [4] analysis for flat-plate cascades operating at low ($M = 0.3$) and moderate ($M = 0.5$) Mach numbers, but the agreement for flat-plates operating at high subsonic Mach number ($M = 0.7$) was not satisfactory. It appears that the grid currently used in the numerical unsteady calculation is not adequate for resolving the high wave number acoustic response phenomena that is associated with high steady-flow Mach numbers and high excitation frequencies. Results for the cascades of symmetric NACA 00XX airfoils show reasonable trends with varying blade thickness, and indicate that blade thickness has only a limited impact on the response of a cascade to incident vortical gusts. The blade thickness study also indicates that the present analysis overcomes the mathematical difficulties associated with unsteady vortical perturbations of potential mean flows containing leading edge stagnation points. The numerical results for the cascades of cambered NACA 0006 airfoils show that the effect of mean blade loading, or mean flow turning, on the unsteady aerodynamic response of cascades to vortical excitations can be significant.

More detailed gust response predictions have been presented for the compressor exit guide vane (EGV), the NACA 0006 compressor cascade, and the turbine cascade. These include vorticity and pressure contours that illustrate the manner in which a vortical gust is distorted as it is convected, by the mean flow, through a blade row, and the unsteady pressure response that is excited by the interaction of this gust with the blading. The numerical results for the compressor and turbine cascades serve to demonstrate the current capabilities of the present unsteady analysis and LINFLO computer code for predicting the unsteady pressure

response of cascades operating under high mean load conditions and at high subsonic inlet Mach number.

The analysis described in this report provides very efficient predictions of the pressure response of realistic cascade configurations to unsteady aerodynamic and structural excitations. Therefore, this analysis should be useful for turbomachinery aeroelastic and aeroacoustic design investigations. Improvements are still needed so that high wave number acoustic response phenomena can be resolved and the potential-equation source term can be accurately determined over broad ranges of excitation frequency and interblade phase angle. Also, in future work, the composite-mesh solution capability of Ref. [19] should be applied to the gust response problem so that entropic and vortical perturbations of discontinuous transonic mean flows can also be analyzed. Finally, the LINFLO code should be coupled to the new steady potential code, currently being developed under a joint NASA Lewis/UTRC research effort, so that the unsteady pressure response of cascades that are representative of those found in the Space Shuttle Main Engine, i.e., cascades that operate at low Mach numbers but induce very high mean-flow deflections, can be analyzed.

References

1. Whitehead, D. S., "Classical Two-Dimensional Methods," *AGARD Manual on Aeroelasticity in Axial-Flow Turbomachines*, Vol. 1, *Unsteady Turbomachinery Aerodynamics*, M. F. Platzer and F. O. Carta (eds.), AGARD–AG–298, March 1987, Chap. III.

2. Whitehead, D. S., "Vibration and Sound Generation in a Cascade of Flat Plates in Subsonic Flow," Cambridge Univ. Engineering Department Report CUED/A–Turbo/TR 15, Cambridge, UK, 1970.

3. Kaji, S. and Okazaki, T., "Propagation of Sound Waves Through a Blade Row, II. Analysis Based on the Acceleration Potential Method," *Journal of Sound and Vibration*, Vol. 11, No. 3, March 1970, pp. 355–375.

4. Smith, S. N., "Discrete Frequency Sound Generation in Axial Flow Turbomachines," British Aeronautical Research Council, R&M 3709, London, UK, 1971.

5. Verdon, J. M., "Further Developments in the Aerodynamic Analysis of Unsteady Supersonic Cascades, I. The Unsteady Pressure Field, II. Aerodynamic Response Predictions," *Trans. ASME, A: Journal of Engineering for Power*, Vol. 99, No. 4, October 1977, pp. 509–525.

6. Nagashima, T. and Whitehead, D. S., "Linearized Supersonic Unsteady Flow in Cascades," British Aeronautical Research Council, R&M 3811, London, UK, 1978.

7. Adamczyk, J. J. and Goldstein, M. E., "Unsteady Flow in a Supersonic Cascade with Subsonic Leading Edge Locus," *AIAA Journal*, Vol. 16, No. 12, December 1978, pp. 1248–1254.

8. Ni, R. H., "A Rational Analysis of Periodic Flow Perturbation in Supersonic Two-dimensional Cascade," *Trans. ASME, A: Journal of Engineering for Power*, Vol. 101, No. 3, July 1979, pp. 431–439.

9. Namba, M., "Three Dimensional Flows," *AGARD Manual on Aeroelasticity in Axial-Flow Turbomachines*, Vol. 1, *Unsteady Turbomachinery Aerodynamics*, M. F. Platzer and F. O. Carta (eds.), AGARD–AG–298, March 1987, Chap. IV.

10. Whitehead, D. S., "The Calculation of Steady and Unsteady Transonic Flow in Cascades," Cambridge Univ. Engineering Dept. Report CUED/A–Turbo/TR 118, Cambridge, UK, 1982.

11. Verdon, J. M. and Caspar, J. R., "A Linearized Unsteady Aerodynamic Analysis for Transonic Cascades," *Journal of Fluid Mechanics*, Vol. 149, December 1984, pp. 403–429.

12. Hall, K. C. and Crawley, E. F., "Calculation of Unsteady Flows in Turbomachinery Using the Linearized Euler Equations," *AIAA Journal*, Vol. 27, No. 6, June,1989, pp. 777–787.

13. Verdon, J. M., "Linearized Unsteady Aerodynamic Theory," *AGARD Manual on Aeroelasticity in Axial Flow Turbomachines*, Vol. 1, Unsteady Turbomachinery Aerodynamics, M. F. Platzer and F. O. Carta (eds.), AGARD–AG–298, March 1987, Chap. II.

14. Verdon, J. M., "Unsteady Aerodynamics for Turbomachinery Aeroelastic Applications," in *Unsteady Transonic Aerodynamics*, D. Nixon (ed.), *Progress in Astronautics and Aeronautics*, Vol. 120, AIAA, Washington, D. C., 1989, pp. 287–347.

15. Acton, E. and Newton, S. G., "Numerical Methods for Unsteady Transonic Flow," *AGARD Manual on Aeroelasticity in Axial-Flow Turbomachines*, Vol. 1, *Unsteady Turbomachinery Aerodynamics*, M. F. Platzer and F. O. Carta (eds.), AGARD–AG–298, March 1987, Chap. VI.

16. Goldstein, M. E., "Unsteady Vortical and Entropic Distortions of Potential Flows Round Arbitrary Obstacles," *Journal of Fluid Mechanics*, Vol. 89, Part 3, December 1978, pp. 433–468.

17. Goldstein, M. E., "Turbulence Generated by the Interaction of Entropy Fluctuations with Non-uniform Mean Flows," *Journal of Fluid Mechanics*, Vol. 93, Part 2, July 1979, pp. 209–224.

18. Caspar, J. R. and Verdon, J. M., "Numerical Treatment of Unsteady Subsonic Flow Past an Oscillating Cascade," *AIAA Journal*, Vol. 19, No. 12, December 1981, pp. 1531–1539.

19. Verdon, J. M. and Usab, W. J., Jr., "Advances in the Numerical analysis of Linearized Unsteady Cascade Flows," U.S. Air Force Report AFWAL–TR–88–2055 (UTRC Report R88–957685–1), prepared under Contract F33615–84–C–2446 for the Department of the Air Force, Air Force Systems Command, August 1988.

20. Atassi, H. M. and Grzedzinski, J., "Unsteady Disturbances of Streaming Motions around Bodies," *Journal of Fluid Mechanics*, Vol. 209, December 1989, pp. 385–403.

21. Verdon, J. M., "The Unsteady Flow in the Far Field of an Isolated Blade Row," *Journal of Fluids and Structures*, Vol. 3, No. 2, March 1989, pp. 123–149.

22. Caspar, J. R., "Unconditionally Stable Calculation of Transonic Potential Flow Through Cascades Using an Adaptive Mesh for Shock Capture," *Trans. ASME, A: Journal of Engineering for Power*, Vol. 105, No. 3, July 1983, pp. 504–513.

23. Whitehead, D. S. and Newton, S. G., "A Finite Element Method for the Solution of Two-Dimensional Transonic Flows in Cascades," *International Journal for Numerical Methods in Fluids*, Vol. 5, February 1985, pp. 115–132.

24. Press, W. H., Flannery, B.P., Teukolsky, S. A. and Vetterling, W. T., *Numerical Recipes: The Art of Scientific Computing*, Cambridge University Press, Cambridge, England, 1986, pp.550–560.

25. Thompson, J. F., Thames, F. C. and Mastin, W., "A Code for Numerical Generation of Boundary-Fitted Curvilinear Coordinate Systems on Fields Containing any Number of Arbitrary Two-Dimensional Bodies," *Journal of Computational Physics*, Vol. 24, No. 3, 1977, pp. 274–302.

26. Abbott, I. H. and Von Doenhoff, A. E., *Theory of Wing Sections*, Dover Publ., New York, 1959.

27. Fransson, T. H. and Suter, P., "Two-Dimensional and Quasi Three-Dimensional Experimental Standard Configurations for Aeroelastic Investigations in Turbomachine-Cascades," Report LTA–TM–83–2, Ecole Polytechnique Federale de Lausanne, Lausanne, Switzerland, 1983.

List of Symbols

All physical parameters listed below are dimensionless. Lengths have been scaled with respect to blade chord, time with respect to the ratio of blade chord to a reference flow speed, density and velocity with respect to a reference density and flow speed, respectively, pressure with respect to the product of the reference density and the square of the reference flow speed, and entropy with respect to a reference value of the fluid specific heat at constant pressure. The reference values of the fluid properties are taken to be their upstream free-stream values. If an equation or figure is given after a symbol description, it is the equation, figure or figure caption in which the symbol first appears.

Roman

$\tilde{\mathcal{A}}$ Vector function of $\mathbf{X} - \mathbf{V}_{-\infty}t$, Equation (4.6).

$\mathcal{A}$ Complex amplitude of $\tilde{\mathcal{A}}$, Equation (4.9).

A Speed of sound in mean or steady background flow, Equation (3.3).

a_0 Constant which describes mean flow behavior in the vicinity of a leading-edge stagnation point, Equation (4.13).

B Mean position of references blade surface, Equation (2.1).

C Blade camber distribution function, Equation (6.2).

D Jacobian determinant for the independent variable transformation $(\Xi, \Psi) \rightarrow (\xi, \eta)$, Equation (5.4).

$d\boldsymbol{\tau}$ differential tangent vector, Equation (4.2).

$d\tau$ Differential length, Equation (4.1).

$\mathbf{e}$ Unit vector, Equation (4.2).

$\mathcal{F}$ Arbitrary scalar or vector function of $\mathbf{X} - \mathbf{V}_{-\infty}t$, Equation (4.4).

F Complex function of the mean-flow stream function, Equation (4.11).

f_y Complex amplitude of first-harmonic unsteady lift, Figure 7.

$\mathbf{G}$ Cascade gap vector $(= G\mathbf{e}_\eta)$, Equation (2.1).

G Blade spacing in "circumferential-" or η-direction; circumferential wave length of an incident disturbance.

30

H_C	Height of circular-arc camber line at blade midchord, Equation (6.2).
H_T	Nominal blade thickness, Equation (6.1).
h_y	Complex amplitude of blade translation normal to chord line, Figure 6.
i	imaginary unit, Equation (2.1).
M	Mach number in steady background flow, Equation (3.3).
m	Blade number index, Equation (2.1).
$\mathbf{n}$	unit normal vector, Equation (3.7).
$\mathcal{P}, \mathcal{Q}$	Grid control function, Equation (5.2), (5.3).
P	Pressure in mean or steady background flow, Equation (3.3).
$\tilde{p}$	First-order unsteady pressure, Equation (2.4).
p	Complex amplitude of first-harmonic unsteady pressure, Equation (2.4).
$\mathcal{R}$	Surface (blade, wake or shock) displacement vector, Equation (2.1).
R	Radius of circular-arc camber line, Equation (6.2).
$\mathbf{r}$	Complex amplitude of surface displacement vector, Equation (2.1).
Sh	Shock mean position, Equation (3.10).
$\tilde{s}$	First-order unsteady entropy, Equation (2.2).
s	Complex amplitude of first-harmonic unsteady entropy, Equation (2.2).
T	Blade thickness distribution function, Equation (6.1).
t	Time, Equation (2.1).
$\tilde{\mathbf{V}}$	Unsteady velocity, Equation (3.1).
$\mathbf{V}$	Mean or steady velocity, Equation (3.1).
$\tilde{\mathbf{v}}$	First-order unsteady velocity, Equation (3.1).

$\mathbf{v}$	Complex amplitude of first-harmonic unsteady velocity, Equation (3.19).
v_g	Complex amplitude, at $\mathbf{x} = 0$, of incident gust velocity component normal to inlet free-stream direction, Figure 5.
$\tilde{\mathbf{v}}_R, \tilde{\mathbf{v}}'_R$	Rotational component of first-order unsteady velocity, Equation (3.5), (4.10).
$\mathbf{v}_R, \mathbf{v}'_R$	Complex amplitude of first-harmonic unsteady rotational velocity, Equation (3.15), (4.12).
$\mathbf{X}$	Lagrangian coordinate vector, Equation (4.3).
X, Y	Surface coordinate, Equation (6.3).
$\mathbf{x}$	Position vector, Equation (2.1).
x, y	Cartesian coordinate along, normal to blade chord, Figure 1.
W	Wake mean position, Equation (3.8).

Greek

α, β, δ	Coefficients of $(\Xi, \Psi) \to (\xi, \eta)$ coordinate transformation, Equation (5.7).
γ	Fluid specific heat ratio, Equation (3.3).
Δp	Complex amplitude of first-harmonic unsteady pressure difference, Figure 5.
Δ	Drift function, Equation (4.1).
ϵ	Small parameter ($<< 1$).
$\tilde{\zeta}$	First-order unsteady vorticity, Equation (2.3).
ζ	Complex amplitude of first-harmonic unsteady vorticity, Equation (2.3).
Θ	Cascade stagger angle, Figure 1.
θ	Slope of blade camber line, Equation (6.3).
κ	Wave number vector, Equation (2.2).
$\Xi, \mathcal{H}$	Independent variable in computational space, Equation (5.2), (5.3).

ξ, η	Cascade axial, "circumferential" Cartesian coordinate, Figure 1.
$\bar{\rho}$	Density in steady background flow, Equation (3.3).
σ	Interblade phase angle, Equation (2.1).
τ	Unit tangent vector, Equation (3.7).
Φ	Velocity potential of the steady background flow, Equation (3.2).
$\tilde{\phi}, \tilde{\phi}'$	Velocity potential of the irrotational component of the first-order unsteady velocity, Equation (3.6), (4.10).
$\tilde{\phi}^*$	First-order pressure-less or convected potential, Equation (4.10).
ϕ, ϕ'	Complex amplitude of the first-harmonic unsteady velocity potential, Equation (3.17), (4.14).
$\tilde{\phi}_E$	Velocity potential associated with acoustic excitation, Equation (3.16).
$\tilde{\phi}_R$	Velocity potential associated with the far-field acoustic response and the far downstream vortical fluctuation, Equation (3.16).
χ	Coefficient that describes the axial variation of the first-order unsteady potential or pressure in the far field, Equation (3.17).
Ψ	Stream function for mean or steady background flow, Equation (4.2).
Ω	Steady flow angle, Figure 1.
ω	Temporal frequency, Equation (2.1).

Mathematical

$\bar{D}/Dt$	Mean-flow convective derivative operator, Equation (3.4).
$\bar{D}_\omega/Dt$	Convective derivative operator for first-harmonic unsteady flow, Equation (4.14).
$Im\{\ \}$	Imaginary part of { }, Figure 5.
$Re\{\ \}$	Real part of { }, Equation (2.1) and Figure 5.

∇	Gradient operator, Equation (3.2).
$\otimes$	Tensor or dyadic product, Equation (4.6).
$[\![\,]\!]$	Change in a flow quantity at a surface of discontinuity, Equation (3.8).

Subscripts

B	Reference blade surface, Equation (6.3).
EXC	Excitation generated by adjacent upstream blade row.
I	Incident pressure or irrotational velocity disturbance, Equation (2.4).
i, j	Mesh point indices, Equation (5.8).
m	Blade number index, Equation (3.7).
n	Shock number index, Equation (3.10).
$N,\ T\ z,\ \eta$	Direction of vector component; N — normal to inlet free-stream flow direction, Equation (4.1); T — along inlet free-stream direction, Equation (4.3); z — out from the page, Equation (4.2); η — the cascade circumferential direction, Figure 1.
Ref	Reference wake location.
ψ	Along streamline, Equation (4.1).
$-$	Axial location at a finite distance upstream from blade row, point of intersection (ξ_-, η_-) of axial line $\xi = \xi_-$ and reference blade stagnation streamline.
$+$	Axial location at a finite distance downstream from blade row.
$\mp\infty$	Far upstream/downstream value of an unsteady flow quantity, Equation (2.2); inlet/exit free-stream value of a steady flow quantity, Figure 1.
$\sim$	Time-dependent flow quantity, Equation (2.2).

Superscripts

$\mp$	Lower, upper surface of blade, Equation (6.3).
$\prime$	Modified first-order velocity potential or rotational velocity, Equation (4.10).
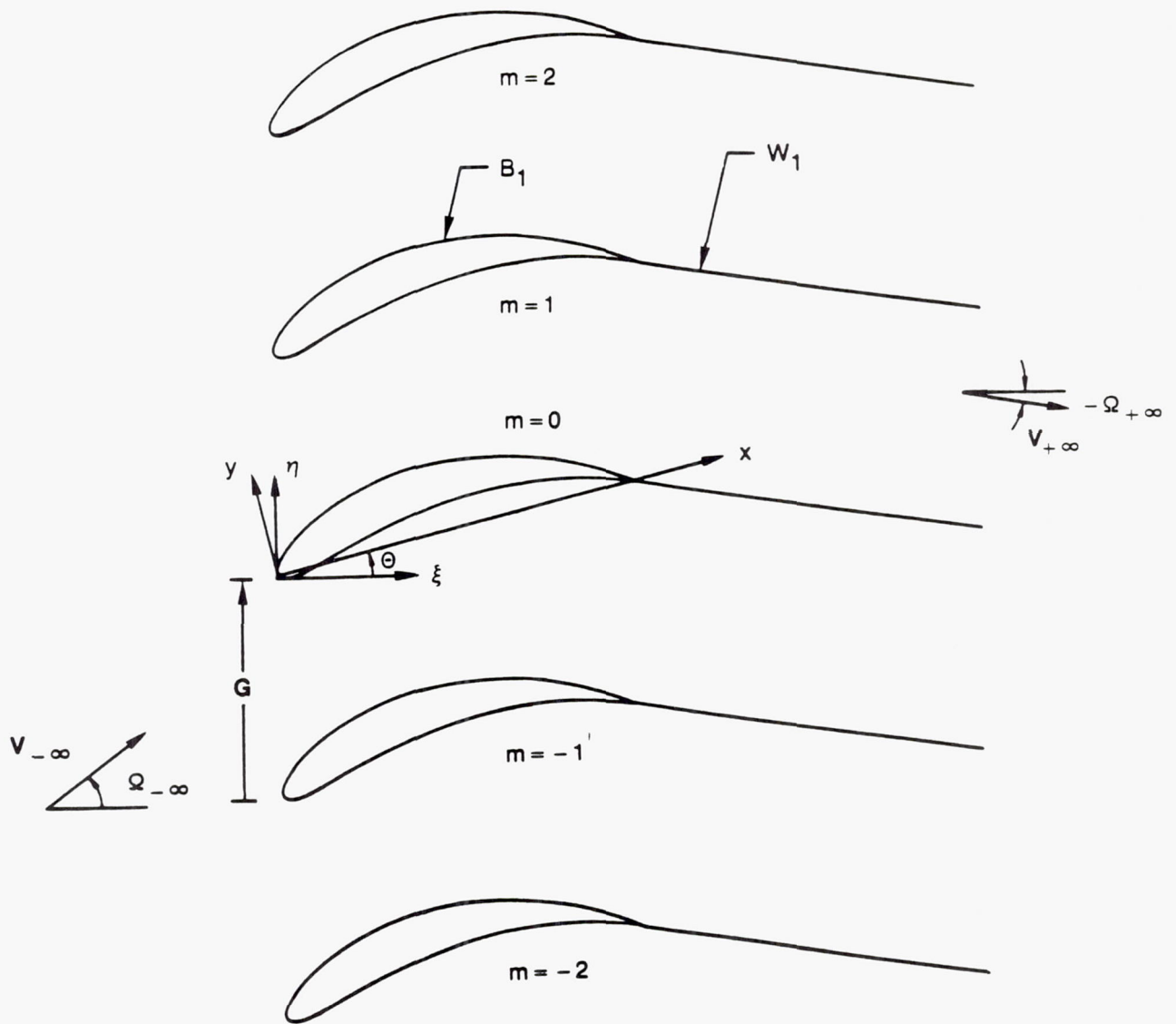
Figure 1. Two-dimensional compressor cascade.
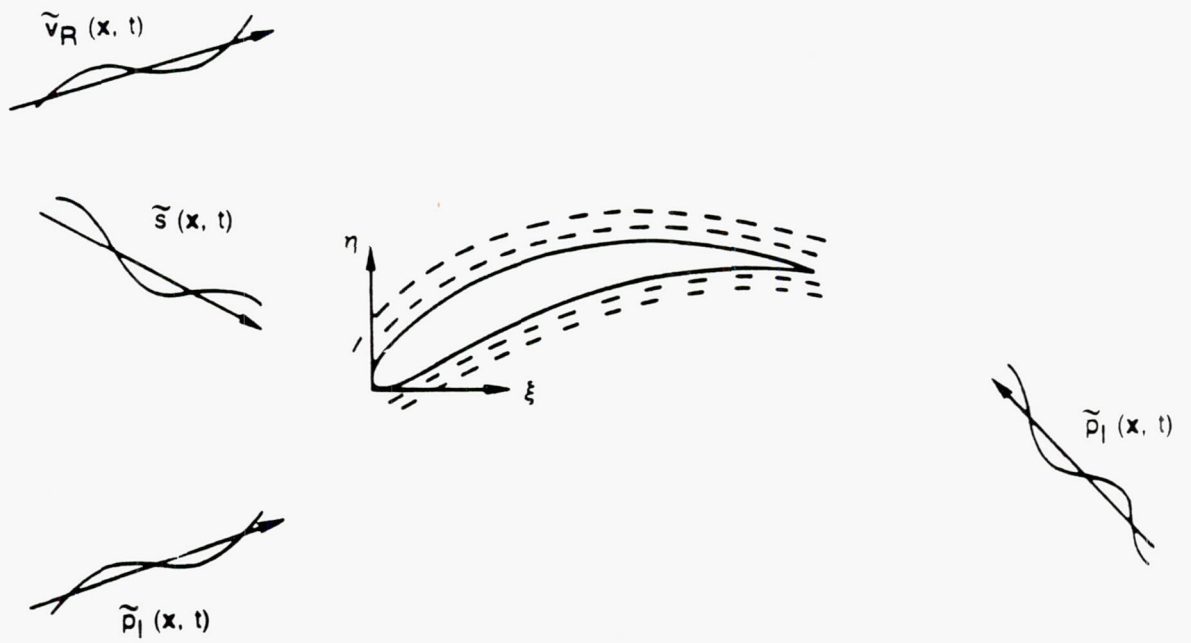
Figure 2. Unsteady excitations: blade motion; incident vortical and entropic disturbances from upstream; and incident acoustic disturbances from upstream and downstream.
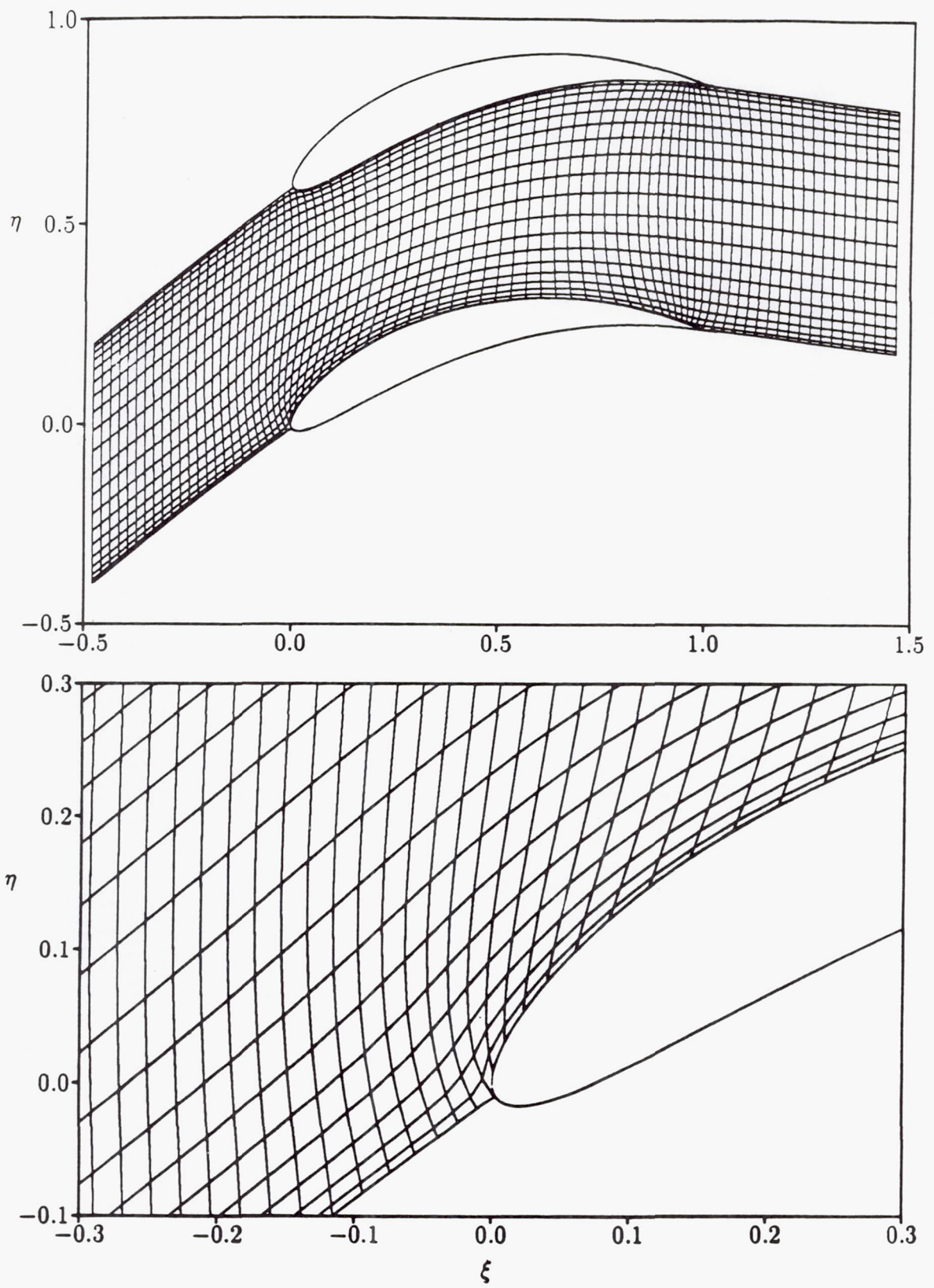
Figure 3. Extended blade-passage solution domain and computational grid.
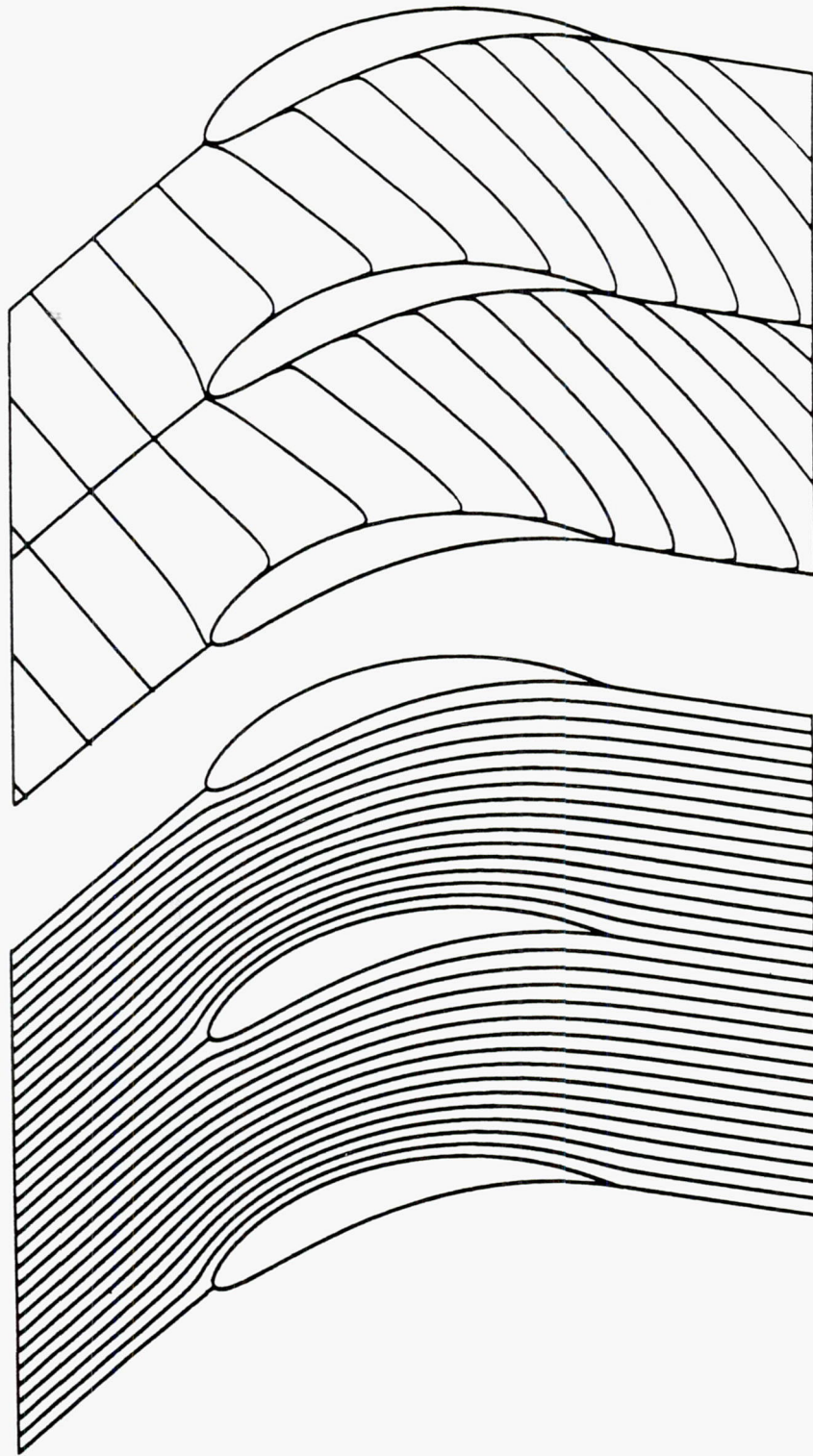
Figure 4. Drift and stream contours for two-dimensional steady cascade flow.
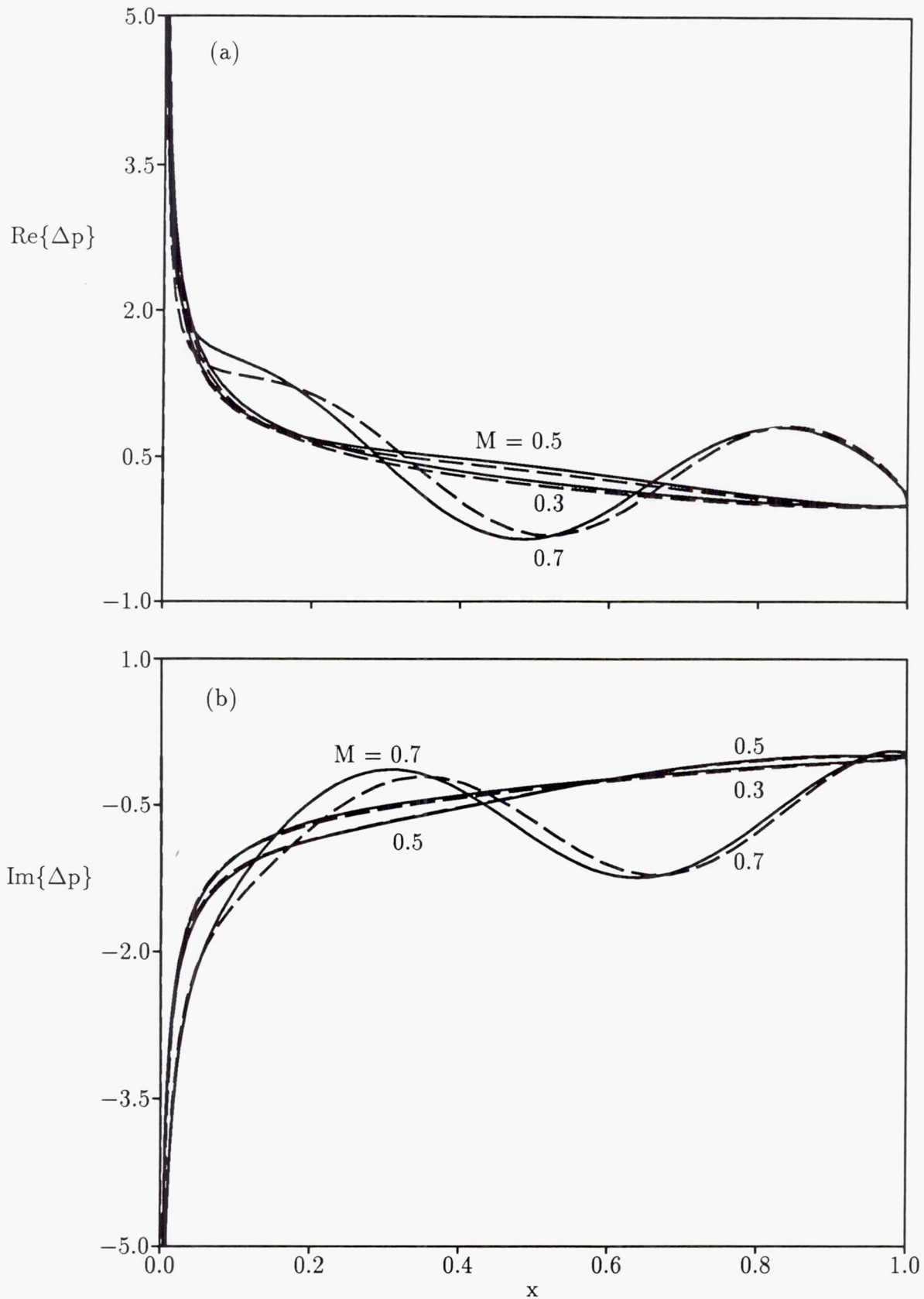
Figure 5. Effect of Mach number on the unsteady pressure-difference response of a flat-plate cascade with $\Omega = \Theta = 45$ deg and $G = 1$ subjected to an incident vortical gust with $v_g = (1, 0)$, $\omega = 5$ and $\sigma = -2\pi$: (a) in-phase component (real part) of Δp, (b) out-of-phase component (imaginary part); $- - -$ Smith analysis (Ref. 4), ——— present analysis.
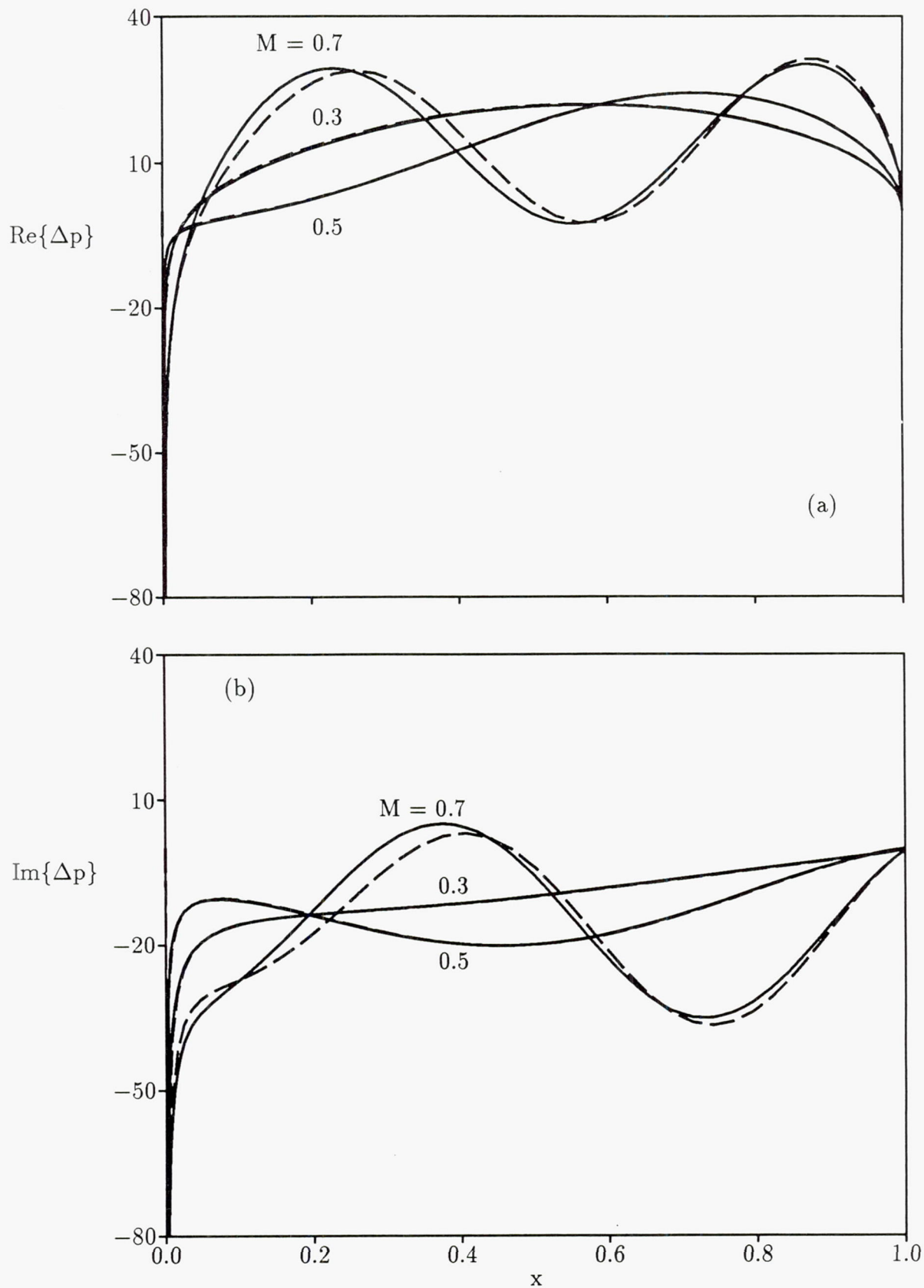
Figure 6. Effect of Mach number on the unsteady pressure-difference response of a flat-plate cascade with $\Omega = \Theta = 45$ deg, $G = 1$ undergoing blade bending vibrations with $h_y = (1,0)$, $\omega = 5$ and $\sigma = -2\pi$: (a), (b), $---$ and $\underline{\qquad}$ as in figure 5.
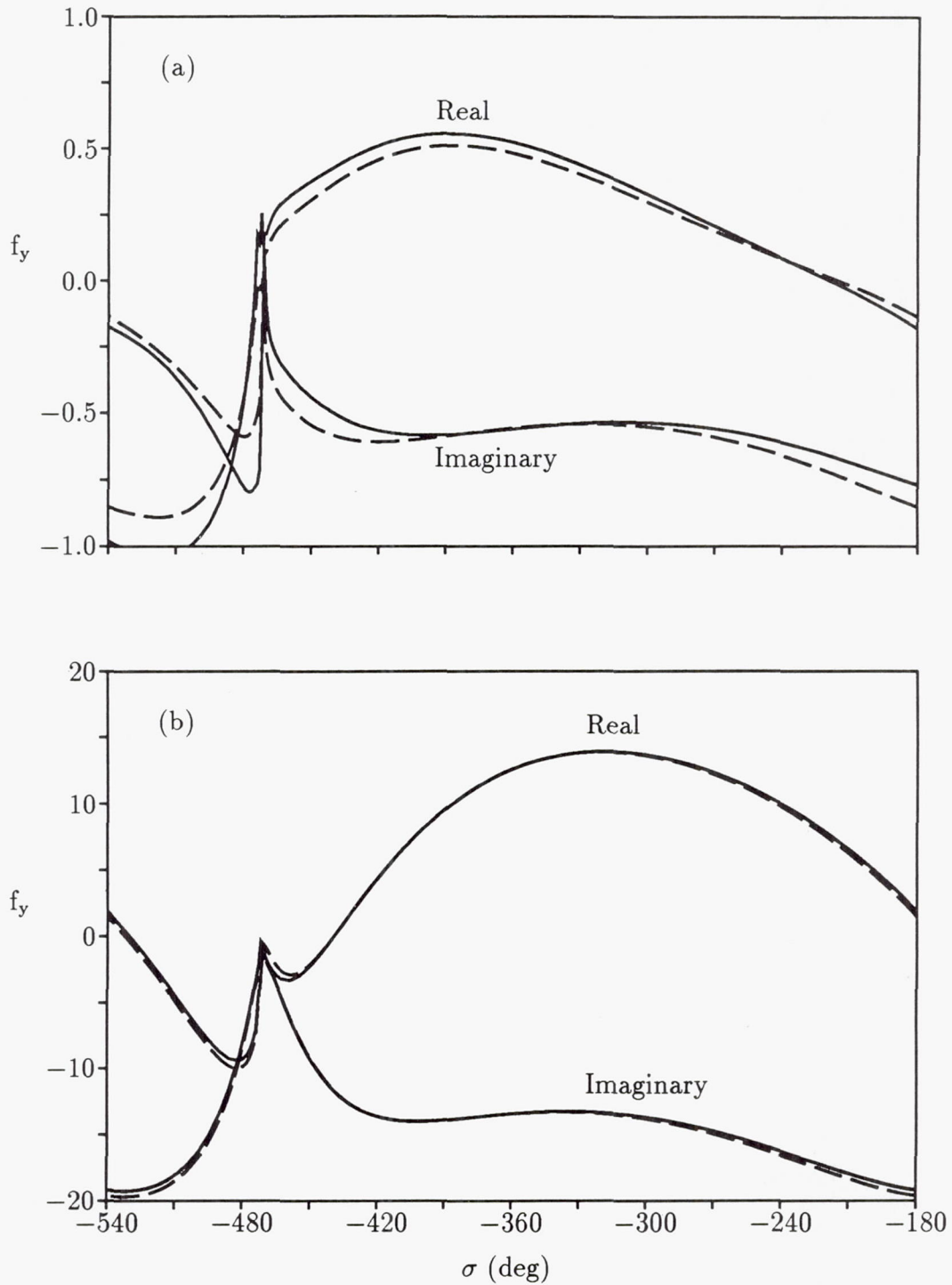
Figure 7. Unsteady lift versus interblade phase angle for a flat-plate cascade with M = 0.3, $\Omega = \Theta = 45$ deg and G = 1: (a) unsteady lift due to incident vortical gusts with $v_g = (1,0)$ and $\omega = 5$; (b) unsteady lift due to blade bending vibrations with $h_y = (1,0)$ and $\omega = 5$; – – – Smith analysis (Ref. 4), ——— present analysis.

41
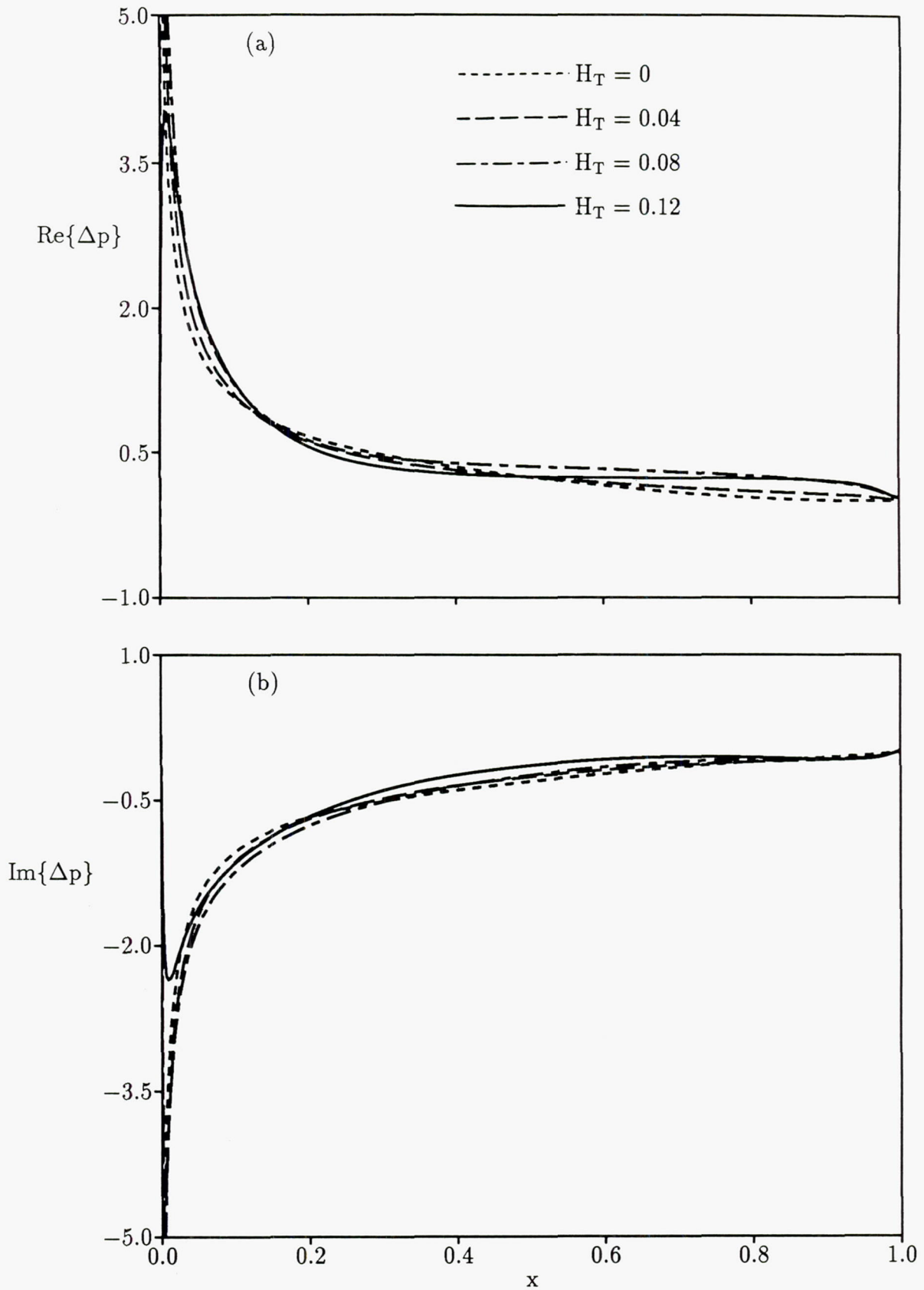
Figure 8. Effect of blade thickness on the unsteady pressure-difference response of NACA 00XX cascades with $M_{-\infty} = 0.3$, $\Omega_{-\infty} = 45$ deg, $\Theta = 45$ deg and $G = 1$ subjected to an incident vortical gust with $v_g = (1,0)$, $\omega = 5$, and $\sigma = -2\pi$: (a) and (b) as in figure 5.
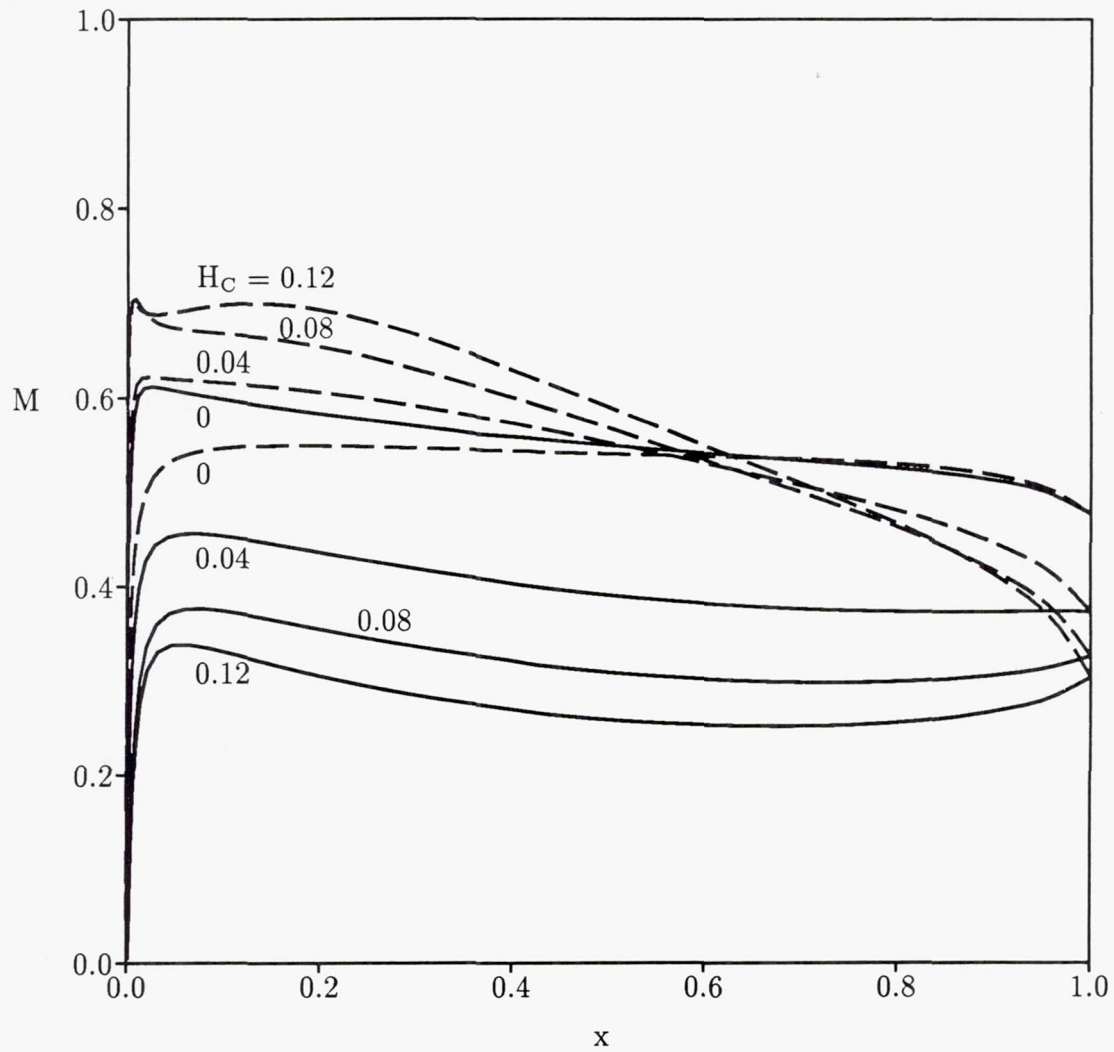
Figure 9 Effect of mean blade loading on the steady Mach number distribution along a blade surface for cascades of cambered NACA 0006 airfoils; − − − upper surface of blade, ——— lower surface.
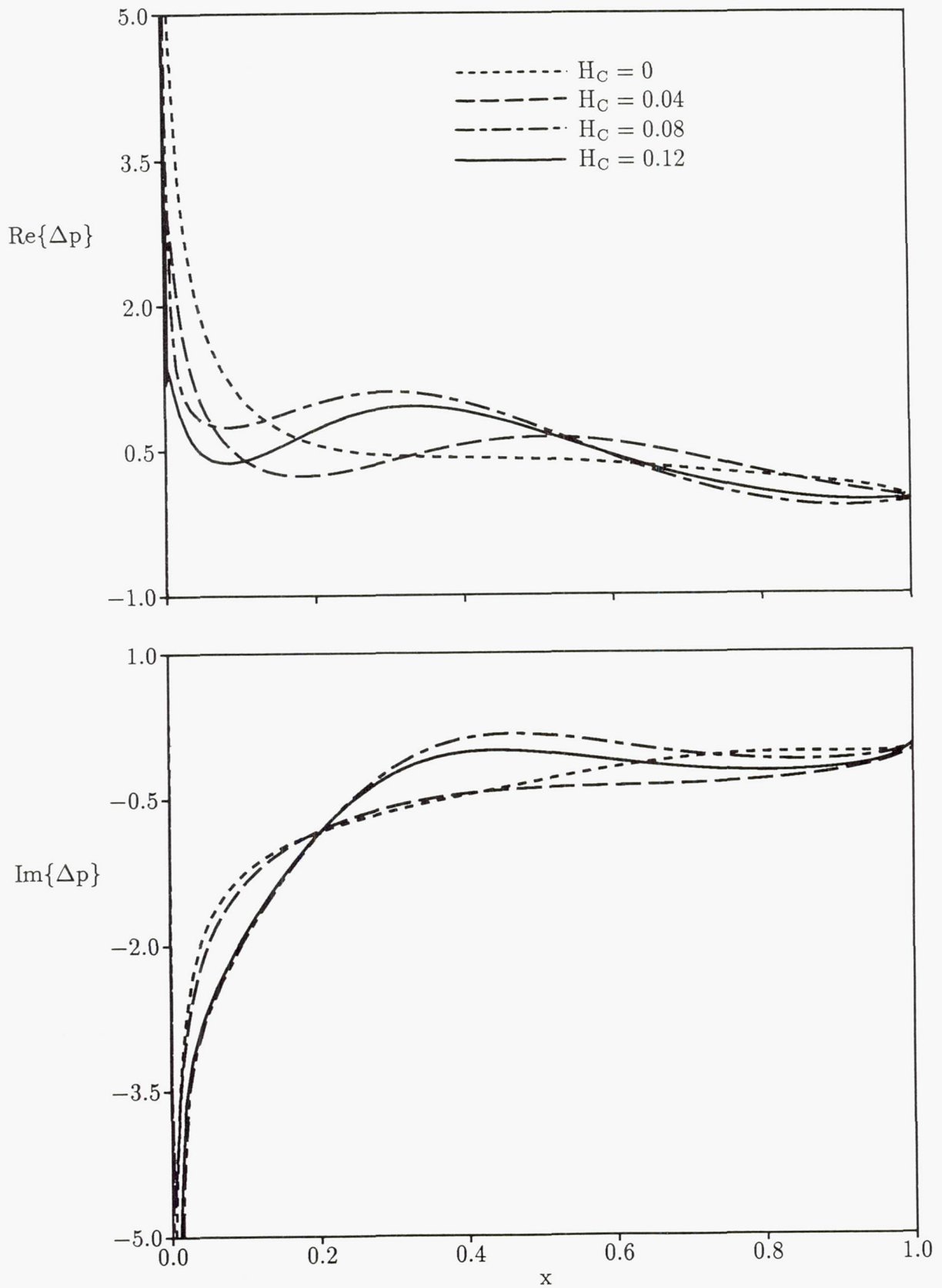
Figure 10. Effect of mean blade loading on the unsteady pressure-difference response for cascades of cambered NACA 0006 blades subjected to an incident vortical gust with $v_g = (1, 0)$, $\omega = 5$ and $\sigma = -2\pi$: (a) and (b) as in figure 5.

44
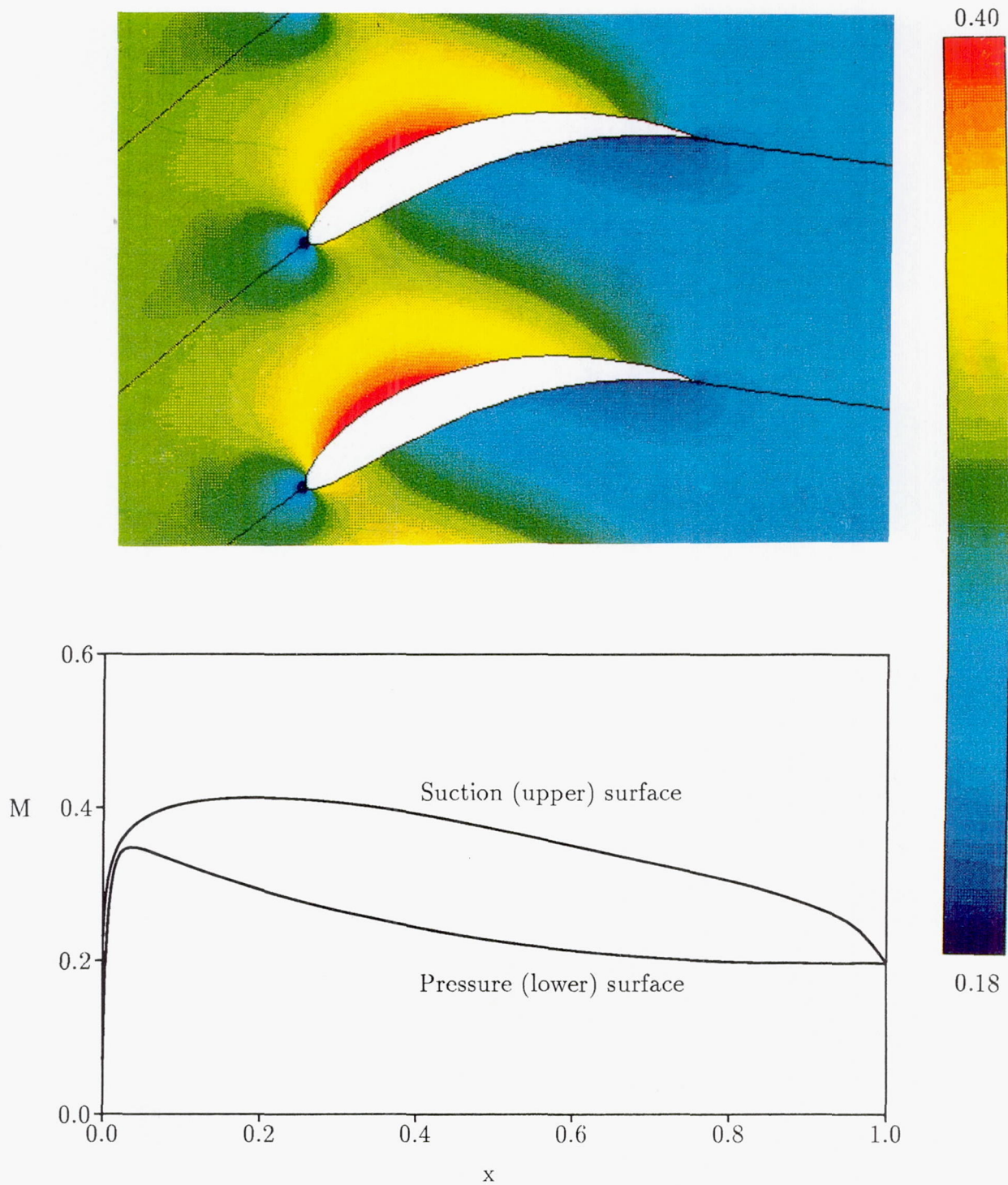
**Figure 11.** Mach number contours and blade surface Mach number distributions for a steady flow with $M_{-\infty} = 0.3$ and $\Omega_{-\infty} = 40$ deg through the EGV cascade ($\Theta = 15$ deg, $G = 0.6$, $H_T = 0.12$ and $H_C = 0.13$).

Figure 12. Contours of the real part of the unsteady vorticity for the EGV and the corresponding flat-plate ($M = 0.3$, $\Omega = \Theta = 40$ deg, $G = 0.6$) cascades subjected to an incident vortical gust with $v_g = (1, 0)$, $\omega = 5$ and $\sigma = -2\pi$.
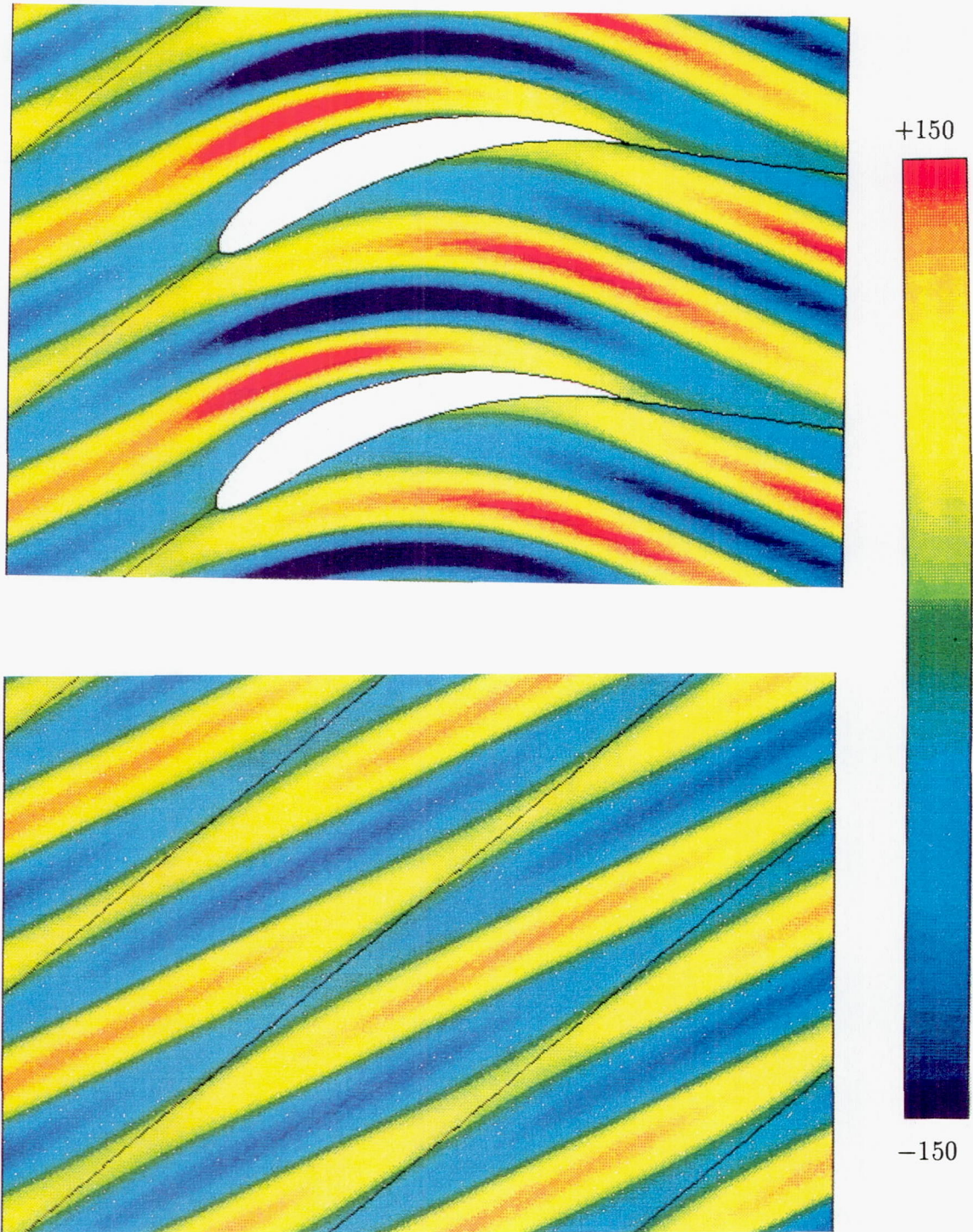
Figure 13. Contours of the real part of the source term for the EGV and the corresponding flat-plate cascades subjected to an incident vortical gust with $v_g = (1,0)$, $\omega = 5$ and $\sigma = -2\pi$.
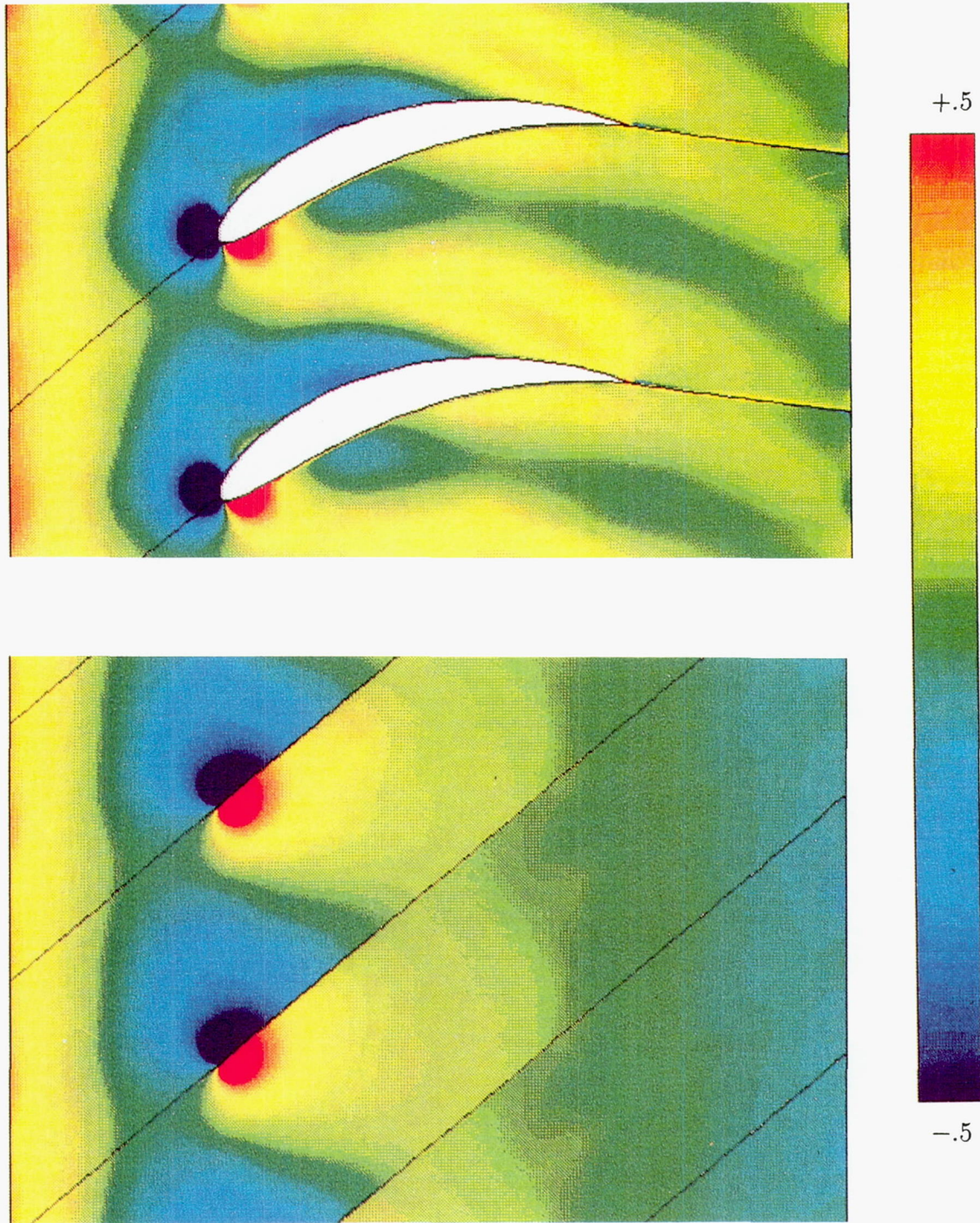
Figure 14. Contours of the in-phase component (real part) of the unsteady pressure for the EGV and the corresponding flat-plate cascades subjected to an incident vortical gust with $v_g = (1, 0)$, $\omega = 5$ and $\sigma = -2\pi$.
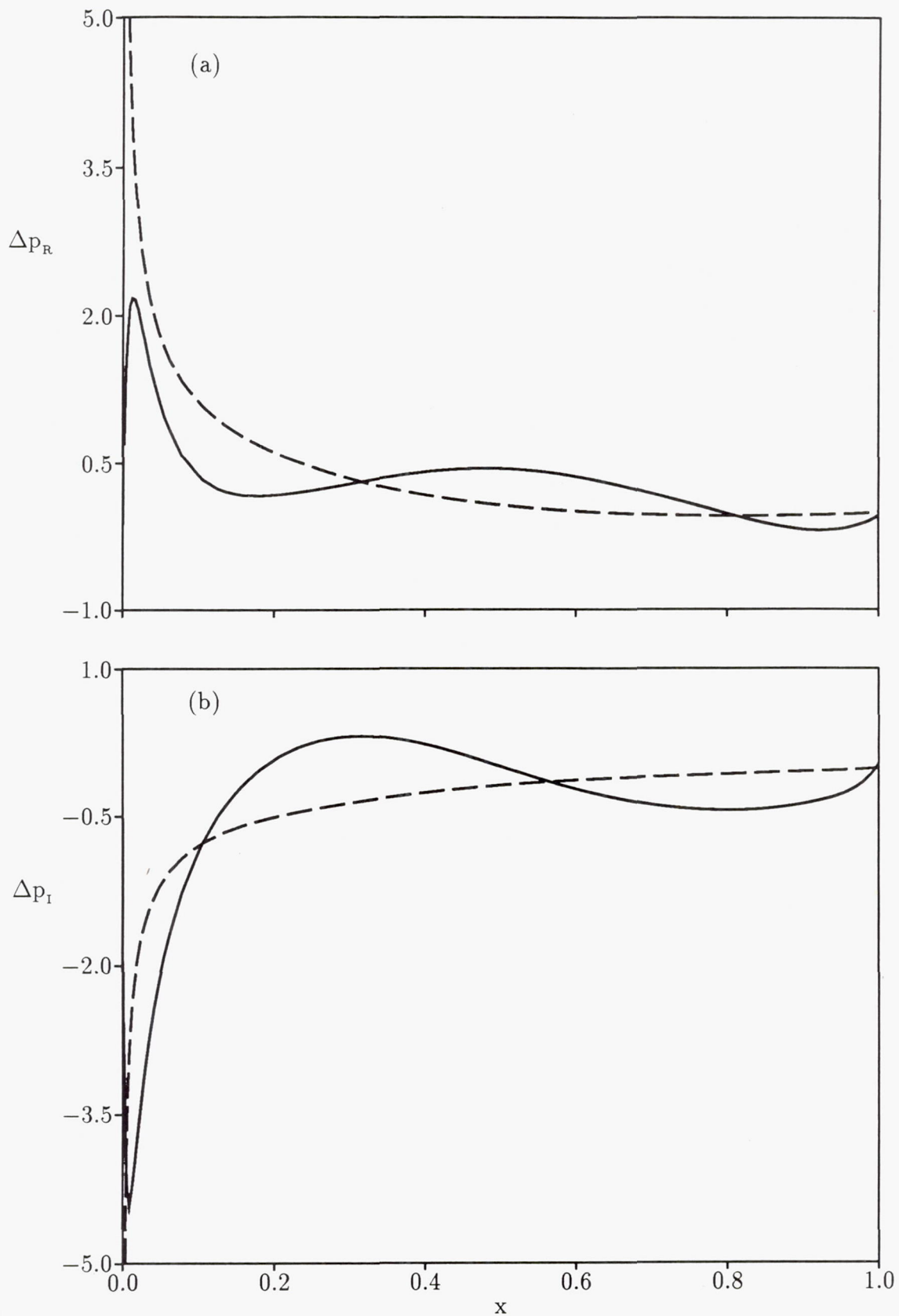
Figure 15. Unsteady pressure-difference response for the EGV and corresponding flat-plate cascades subjected to an incident vortical gust with $v_g = (1, 0)$, $\omega = 5$ and $\sigma = -2\pi$: (a) in-phase component (real part); (b) out-of-phase component (imaginary part); $---$ flat-plate cascade, $\rule{1cm}{0.4pt}$ EGV cascade.

49
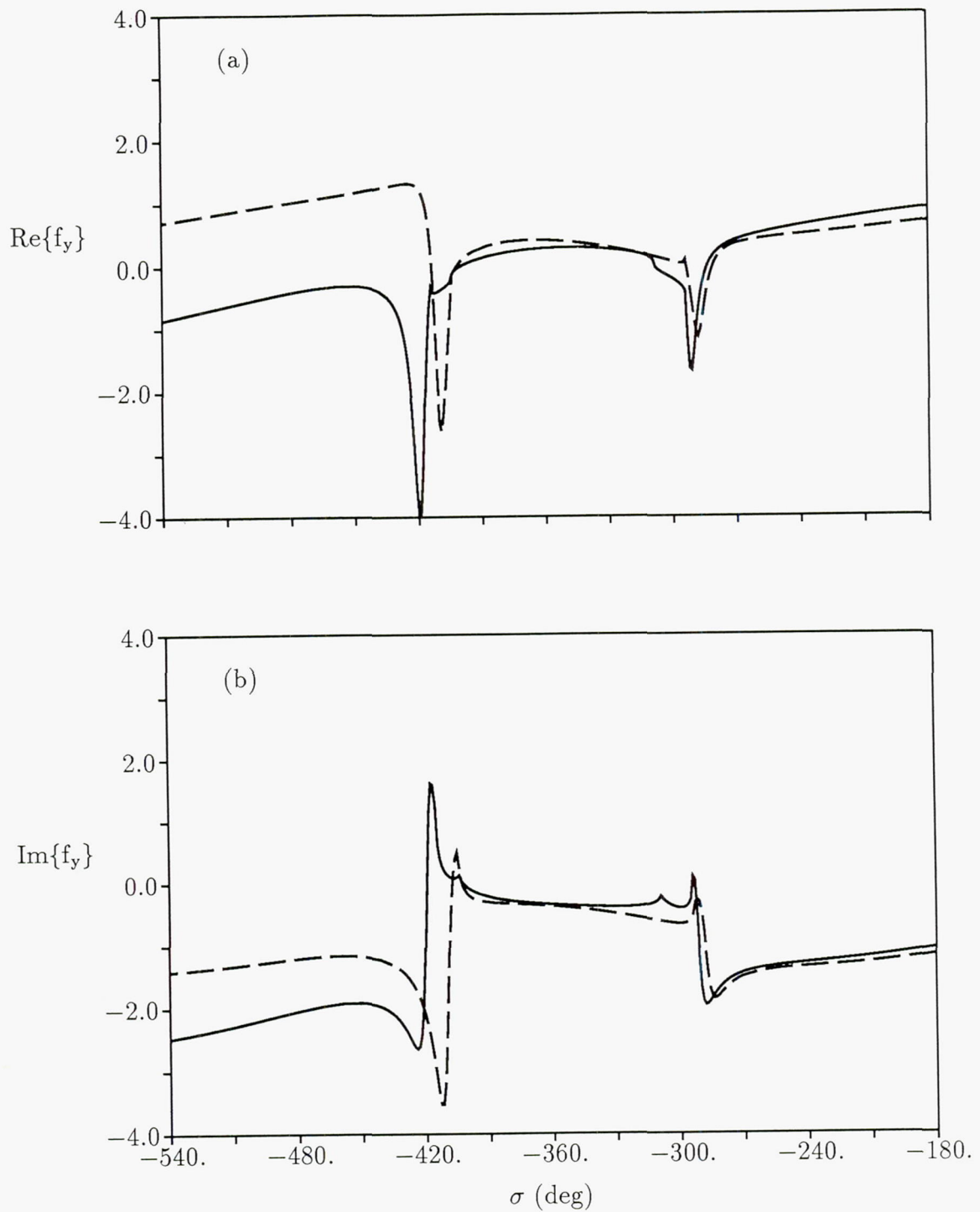
Figure 16. Unsteady lift versus interblade phase angle for the EGV and corresponding flat-plate cascades subjected to incident vortical gusts with $v_g = (1,0)$ and $\omega = 5$: (a), (b), $- - -$ and ——— as in figure 15.
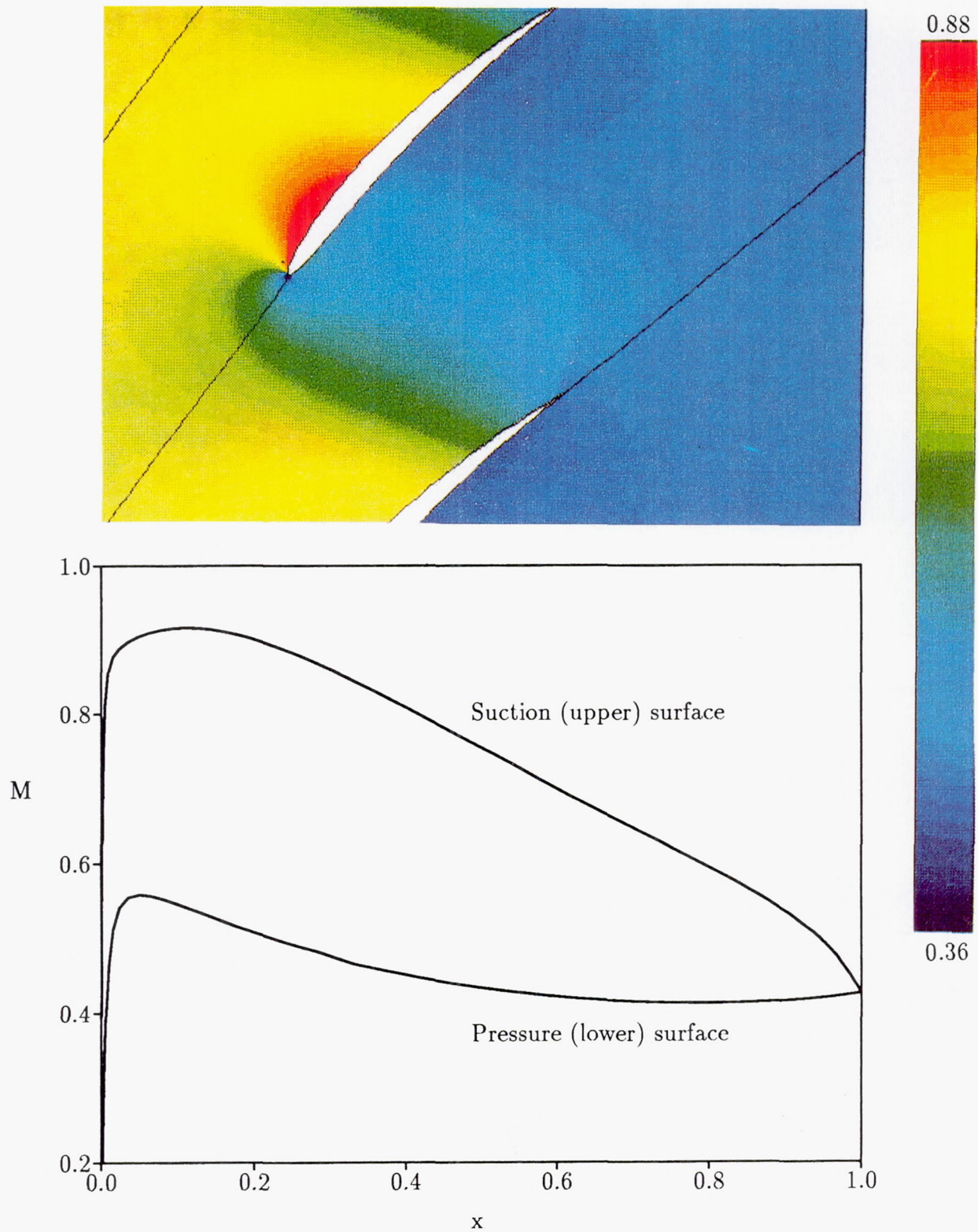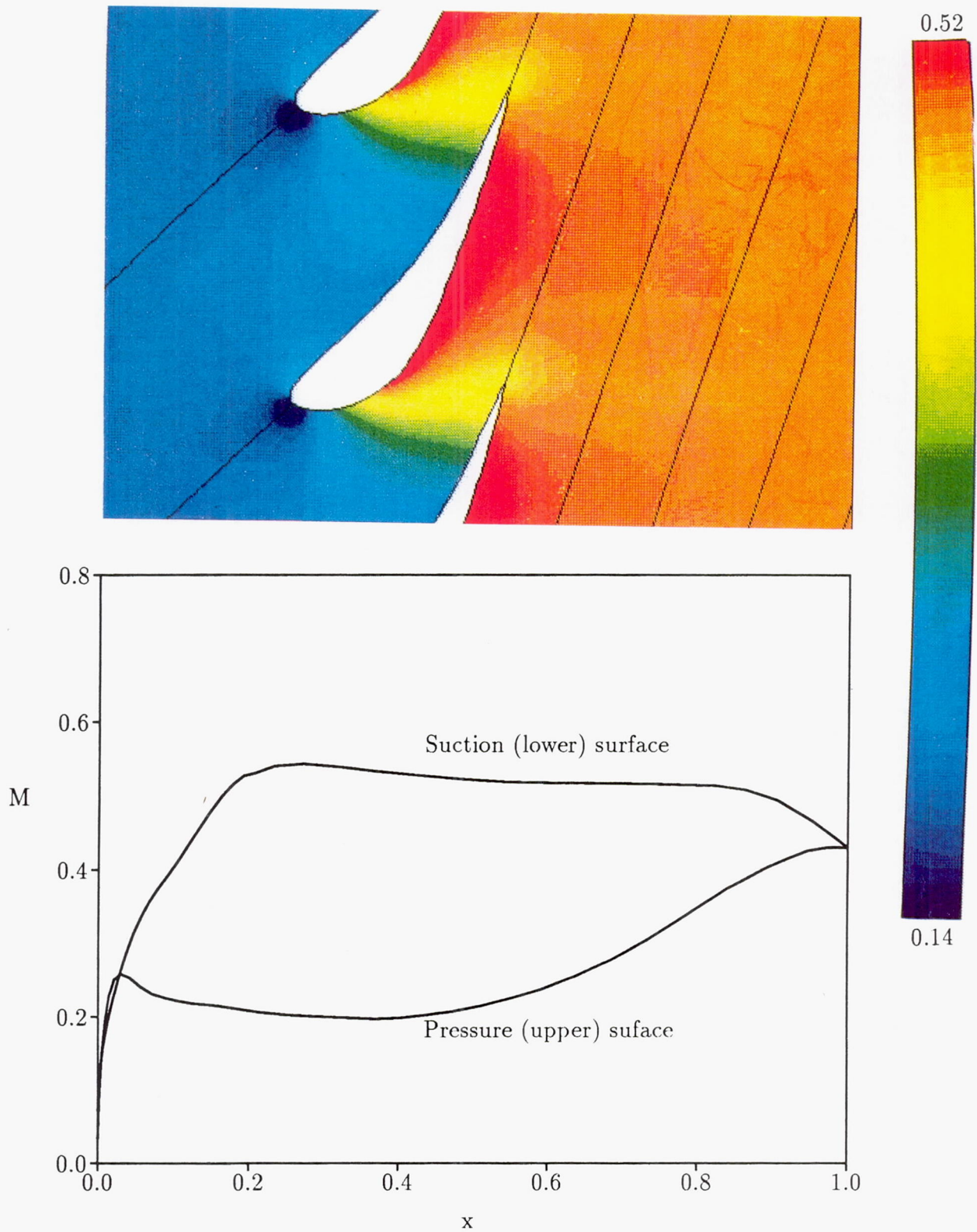
Figure 17. Mach number contours and surface Mach number distributions for steady flow with $M_{-\infty} = 0.7$ and $\Omega_{-\infty} = 55$ deg through the cambered NACA 0006 cascade ($\Theta = 45$ deg, $G = 1.0$, $H_T = 0.06$ and $H_C = 0.05$).
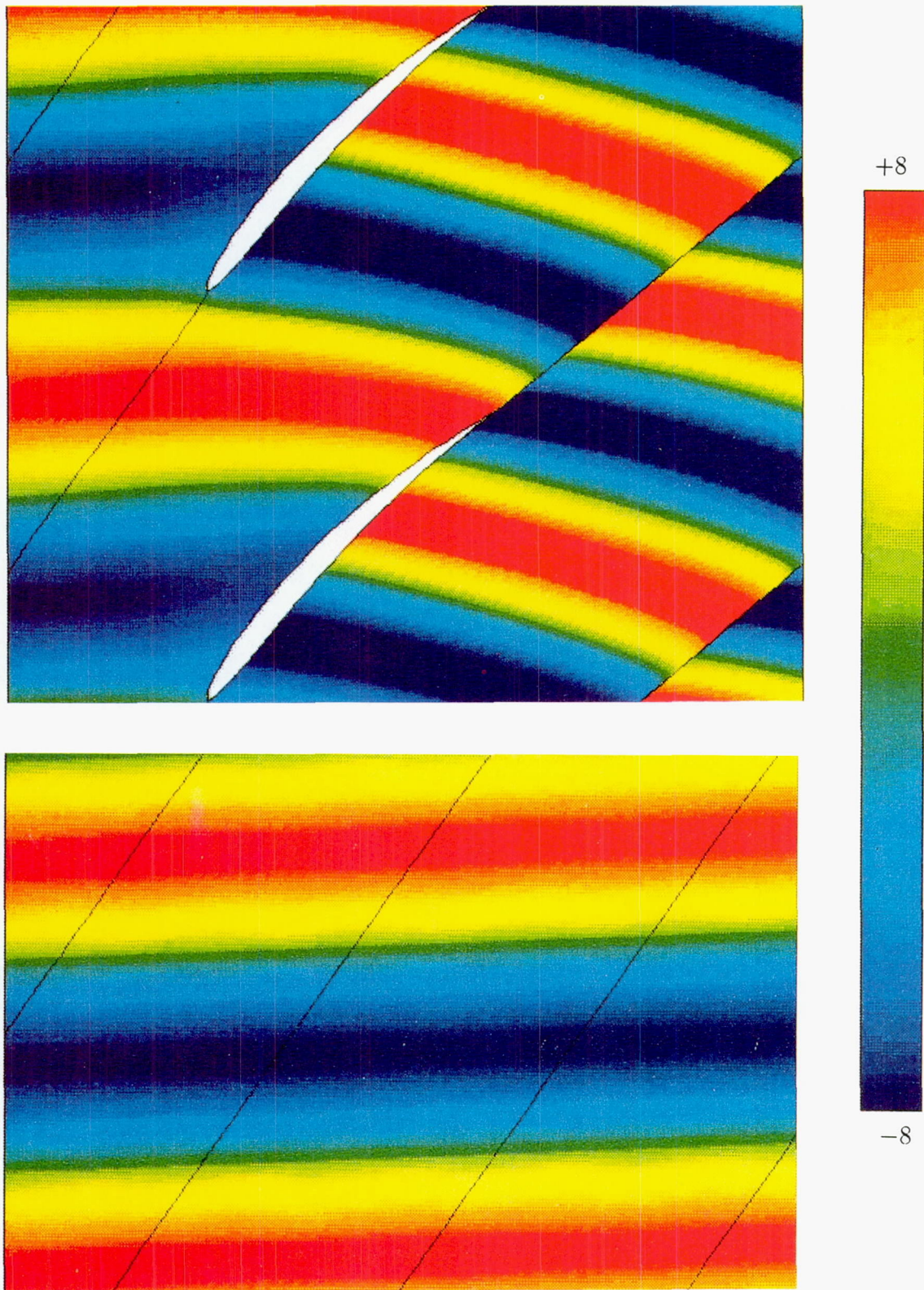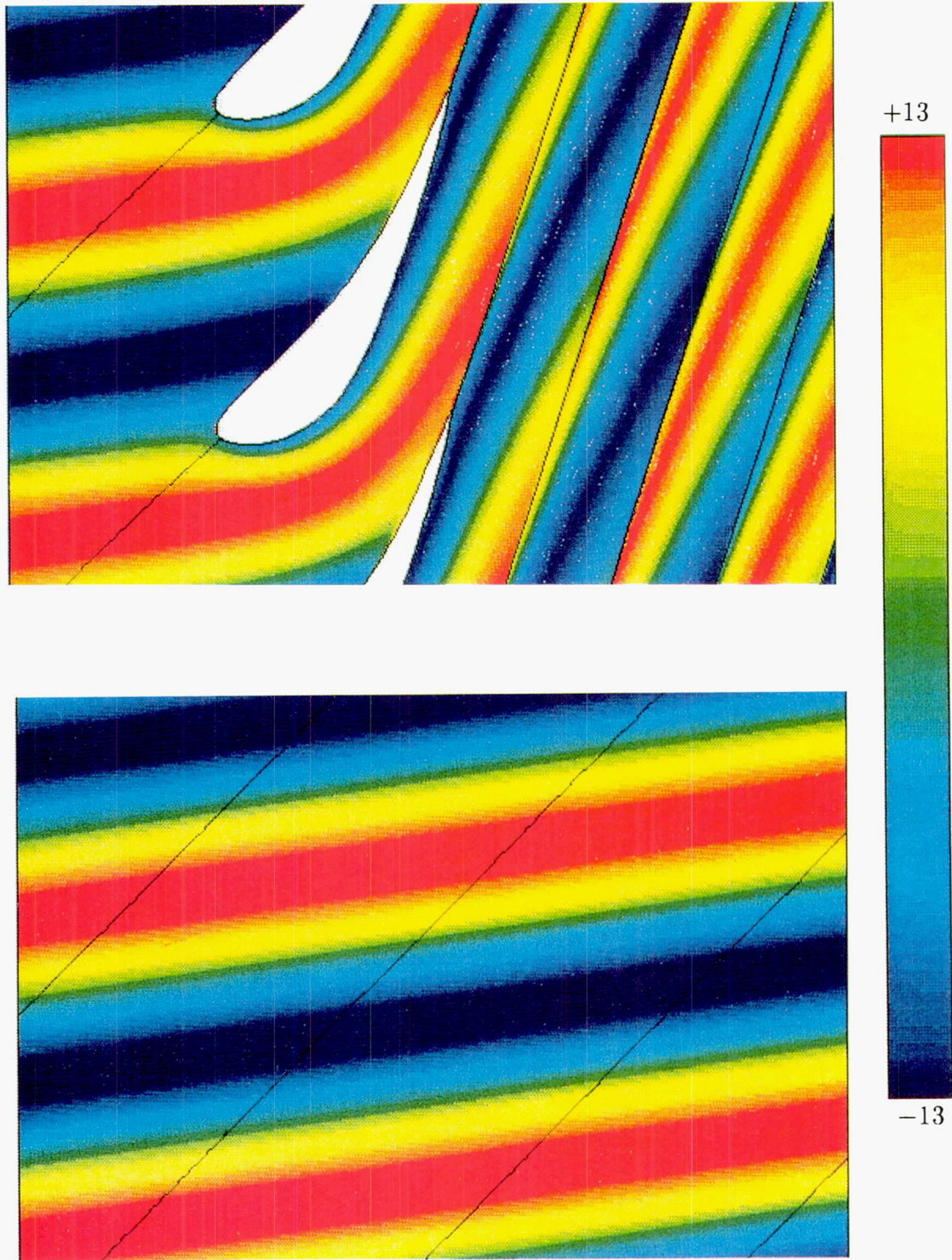
Figure 18. Contours of the real part of the unsteady vorticity for the cambered NACA 0006 and the corresponding flat-plate (M = 0.7, $\Omega = \Theta = 55$ deg, G = 1.0) cascades subjected to an incident vortical gust with $v_g = (1, 0)$, $\omega = 5$ and $\sigma = -2\pi$.
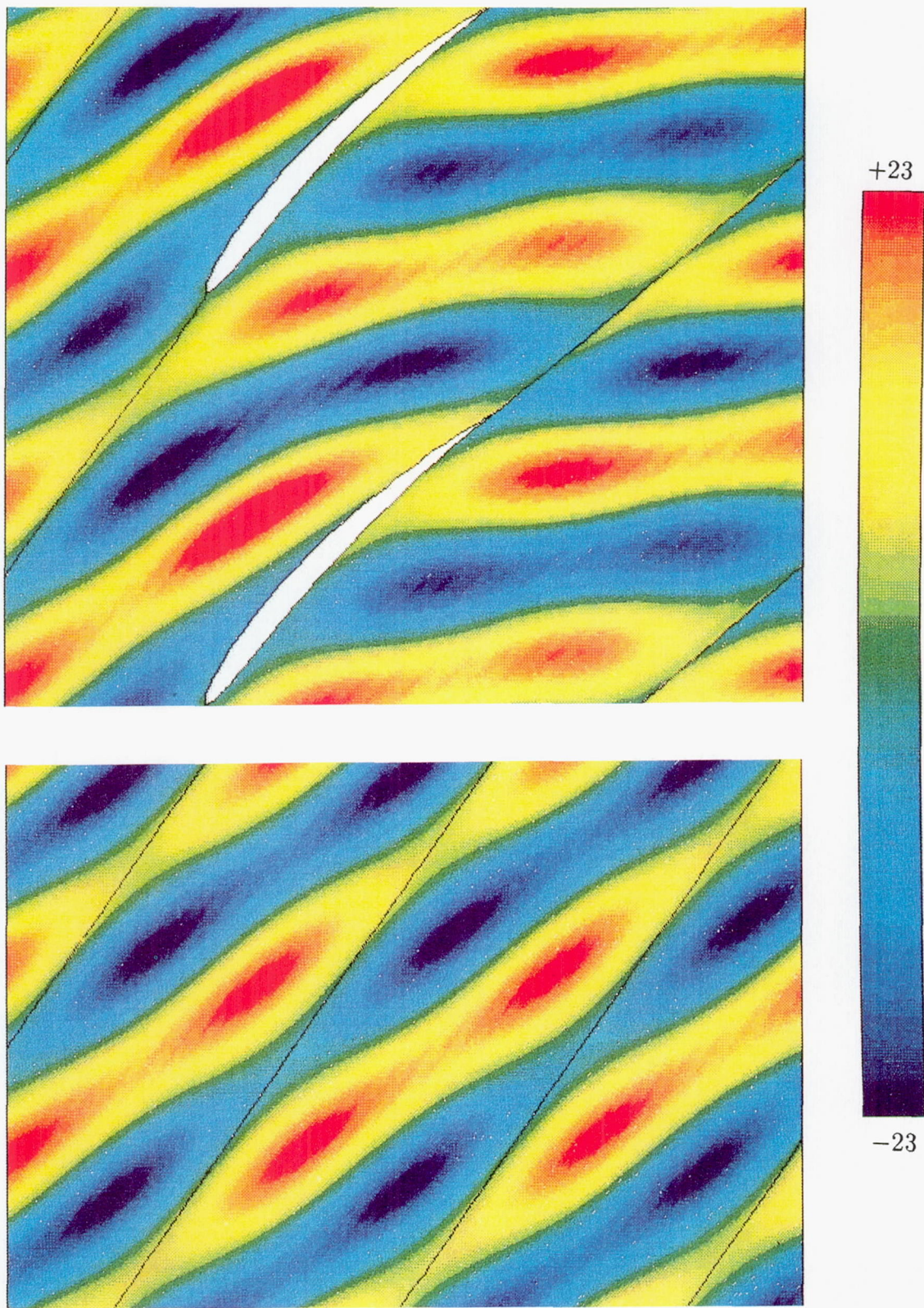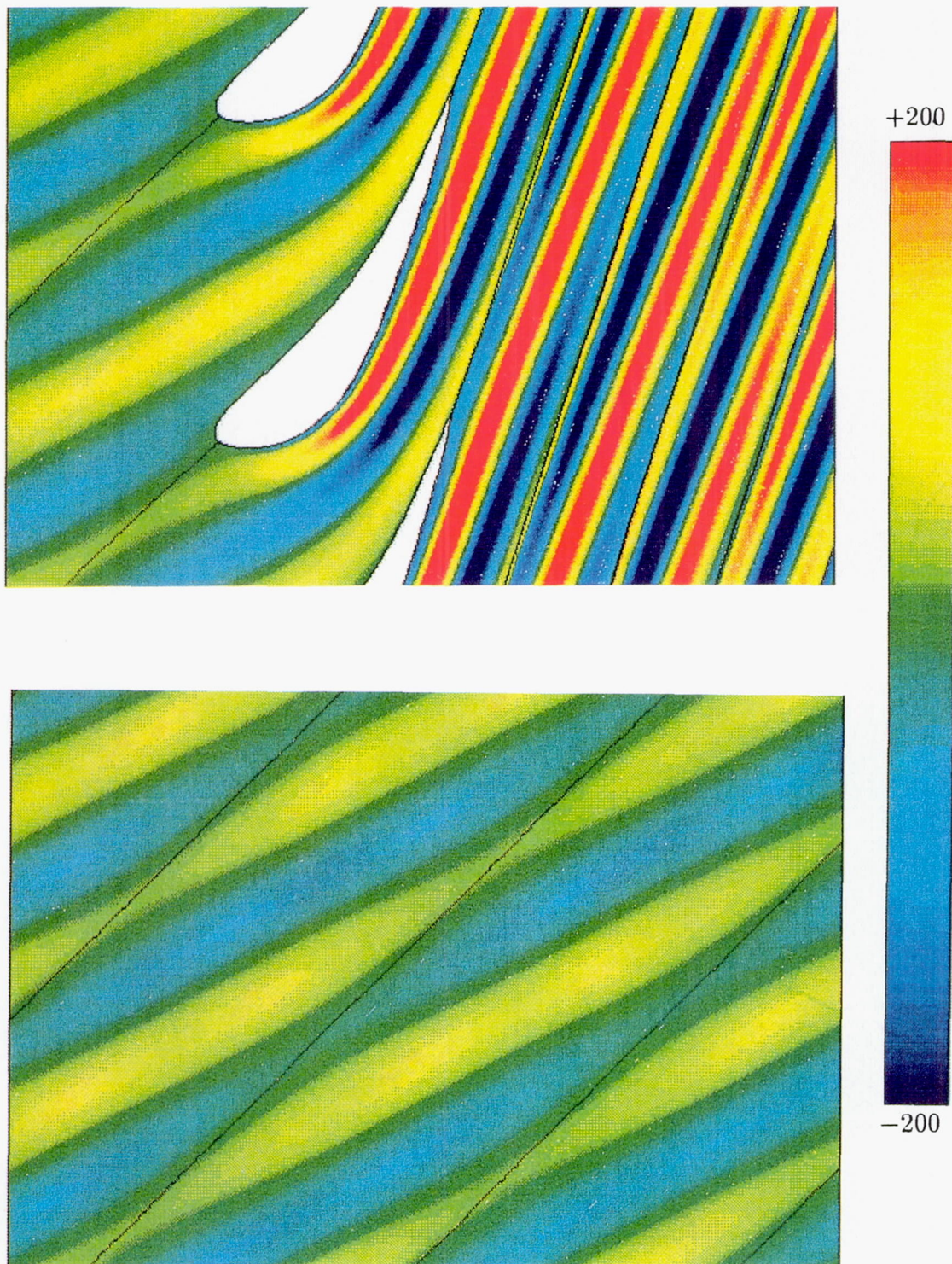
Figure 19. Contours of the real part of the source term for the cambered NACA 0006 and the corresponding flat-plate cascades subjected to an incident vortical gust with $v_g = (1, 0)$, $\omega = 5$ and $\sigma = -2\pi$.

53
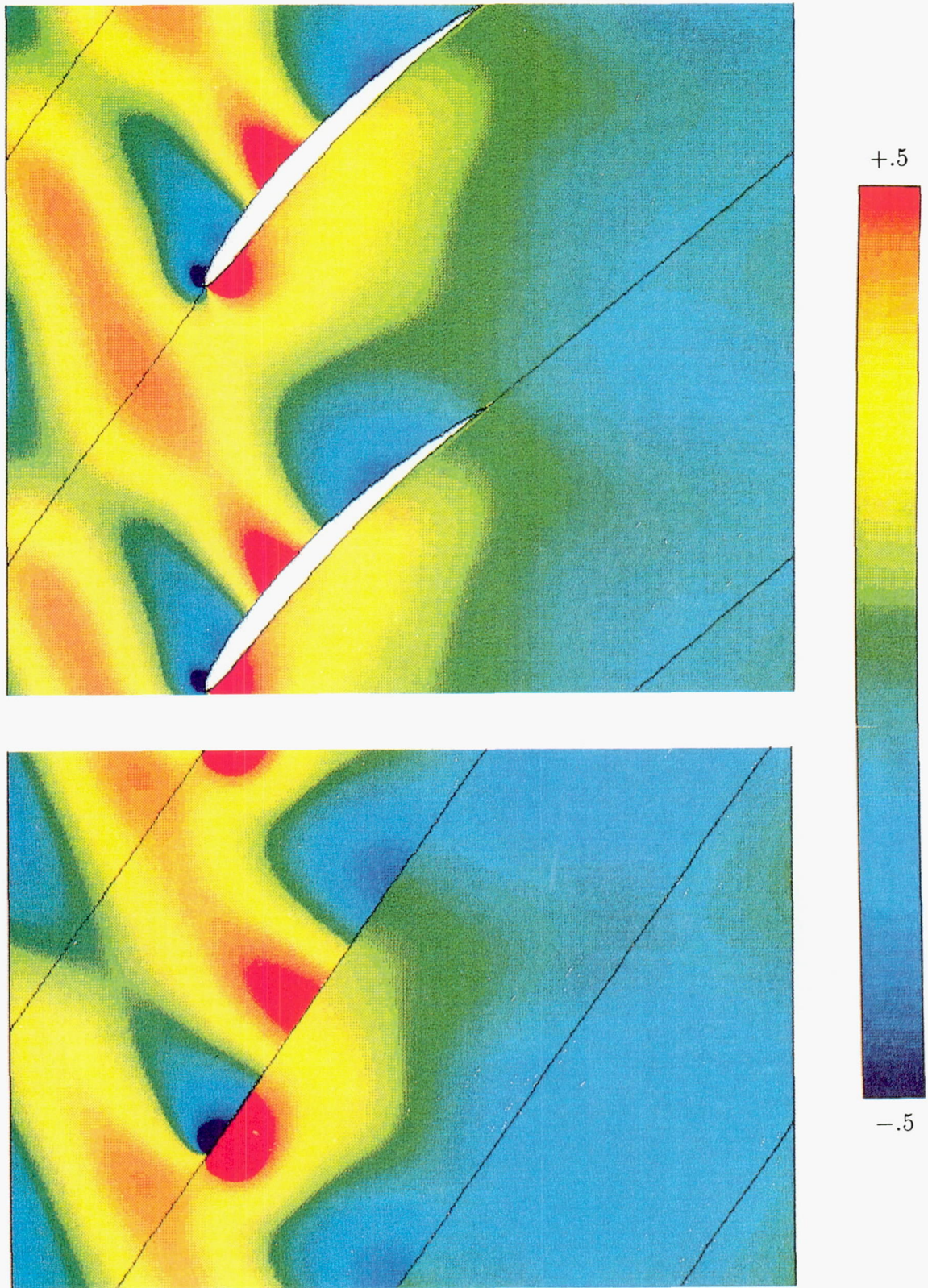
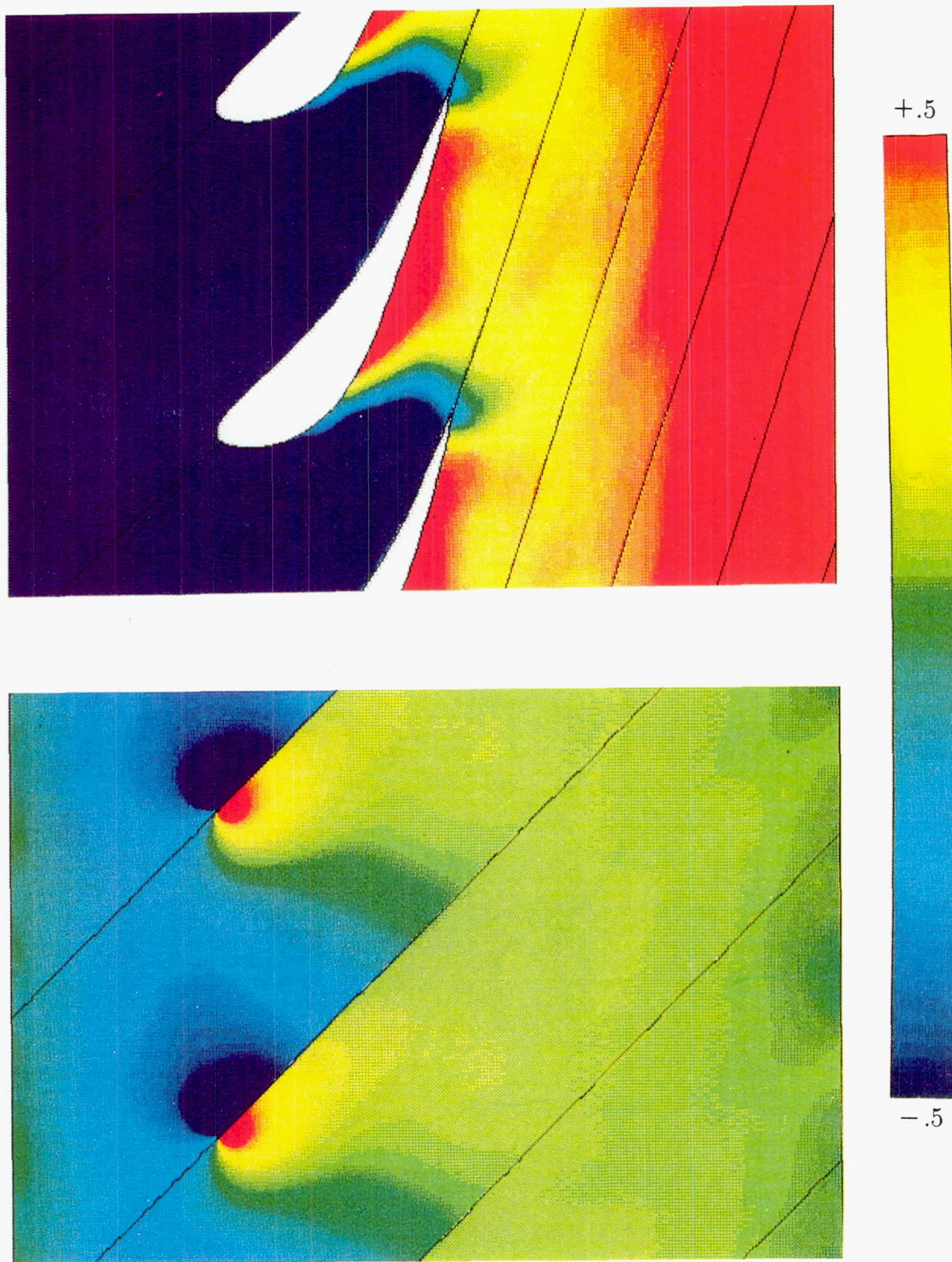**Figure 20.** Contours of the in-phase component (real part) of the unsteady pressure for the cambered NACA 0006 and the corresponding flat-plate cascades subjected to an incident vortical gust with $v_g = (1, 0)$, $\omega = 5$ and $\sigma = -2\pi$.
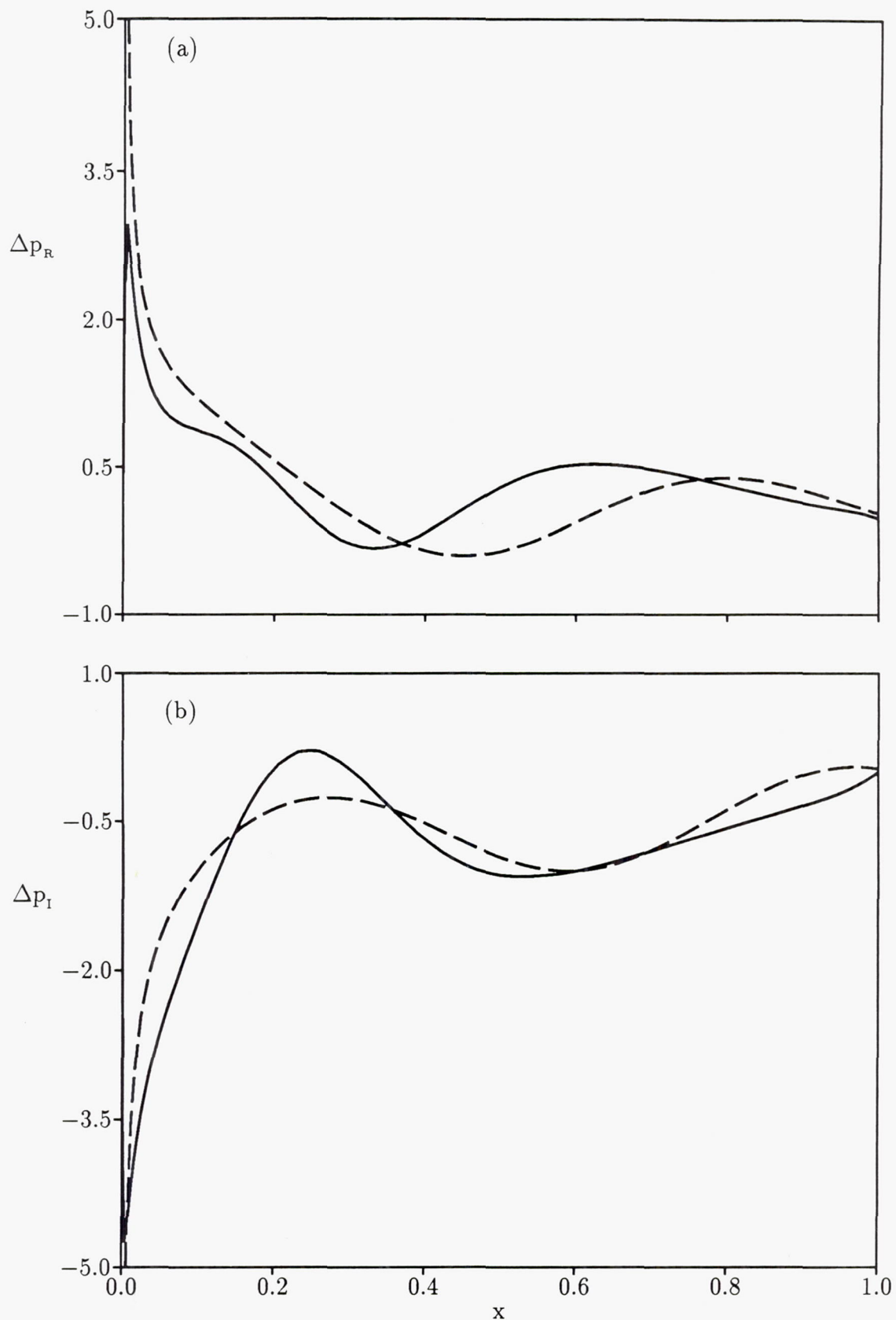
Figure 21. Unsteady pressure-difference response for the cambered NACA 0006 and corresponding flat-plate cascades subjected to an incident vortical gust with $v_g = (1, 0)$, $\omega = 5$ and $\sigma = -2\pi$: (a) in-phase component (real part); (b) out-of-phase component (imaginary part); $- - -$ flat-plate cascade, ———— NACA 0006 cascade.
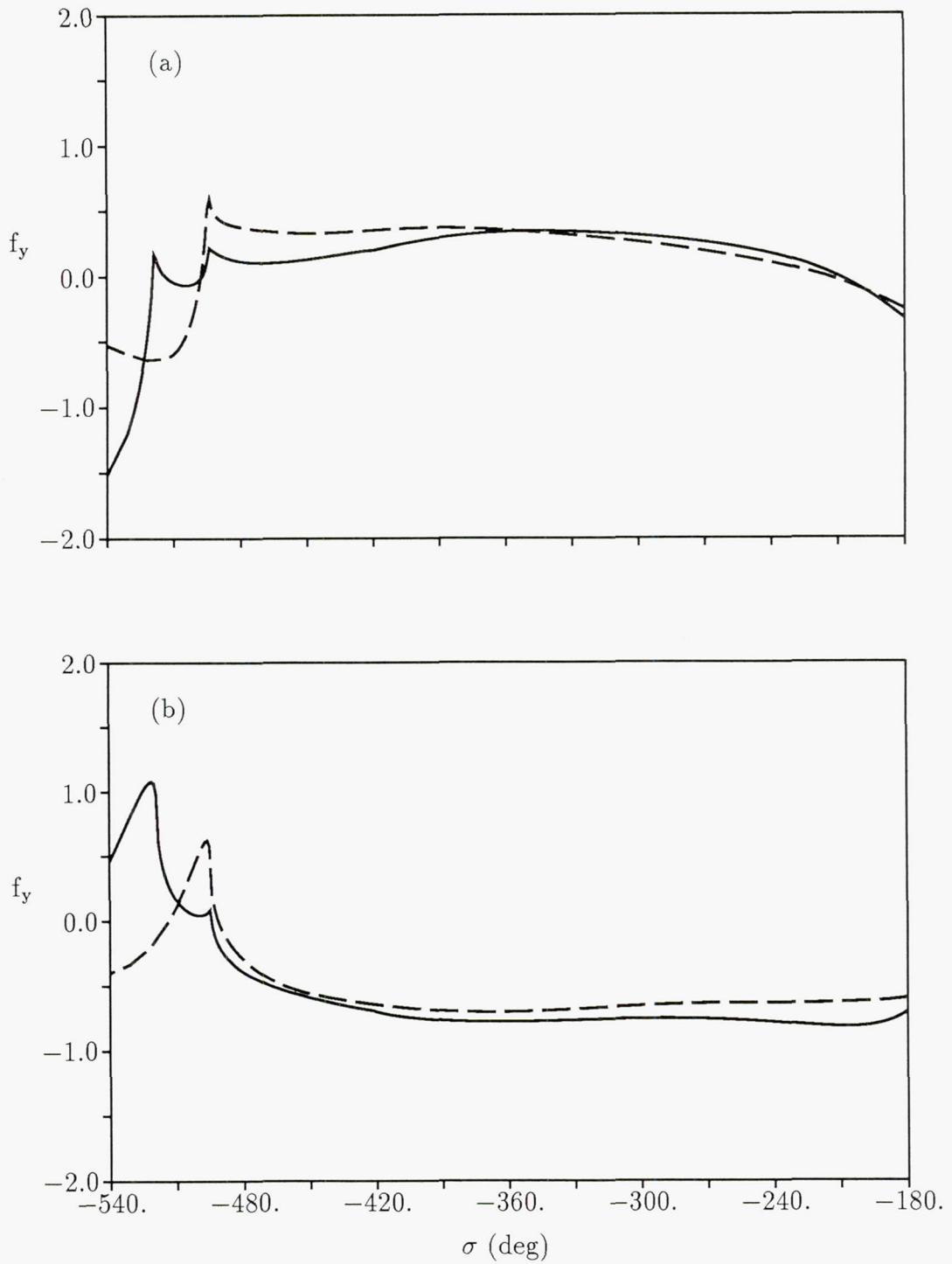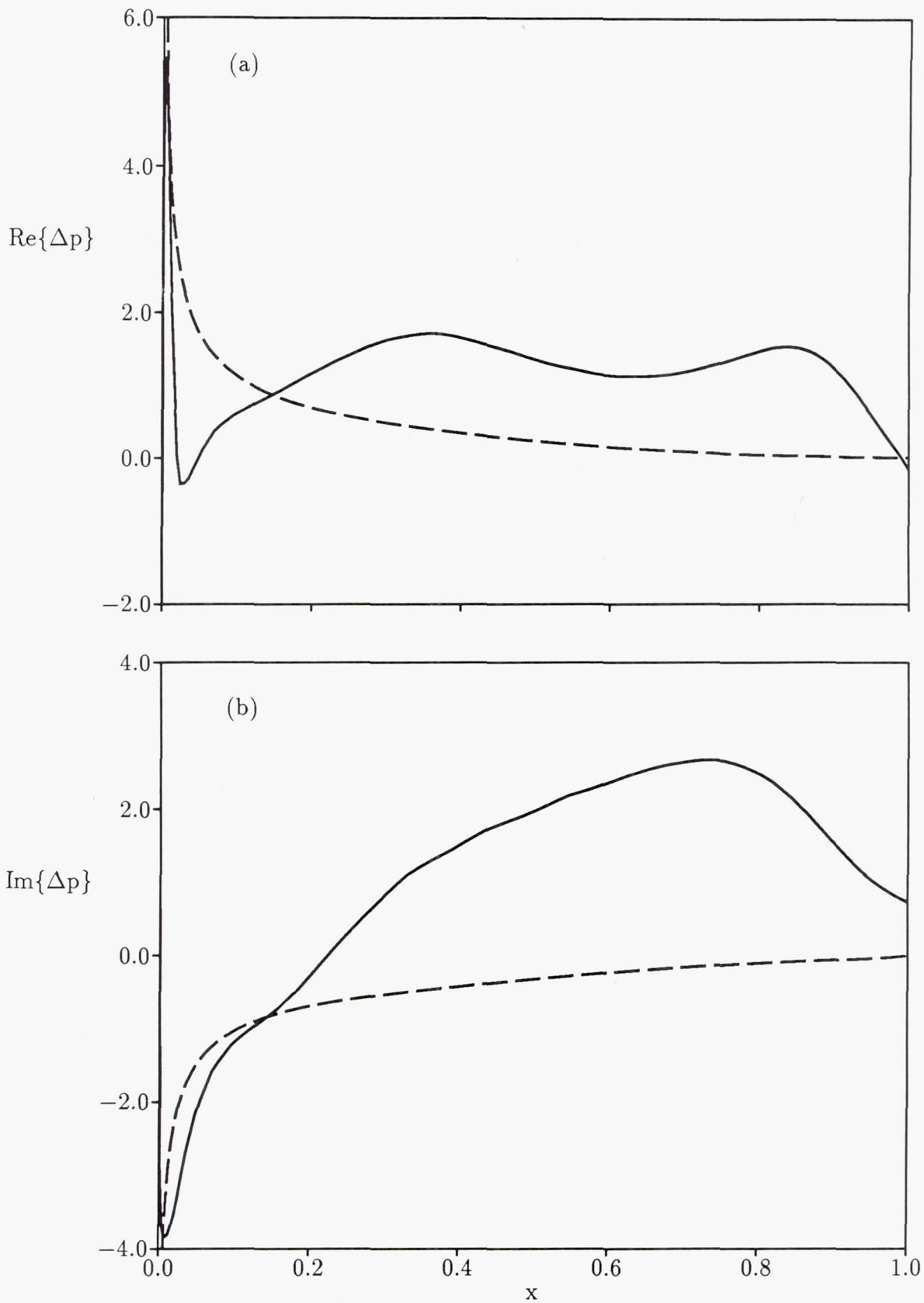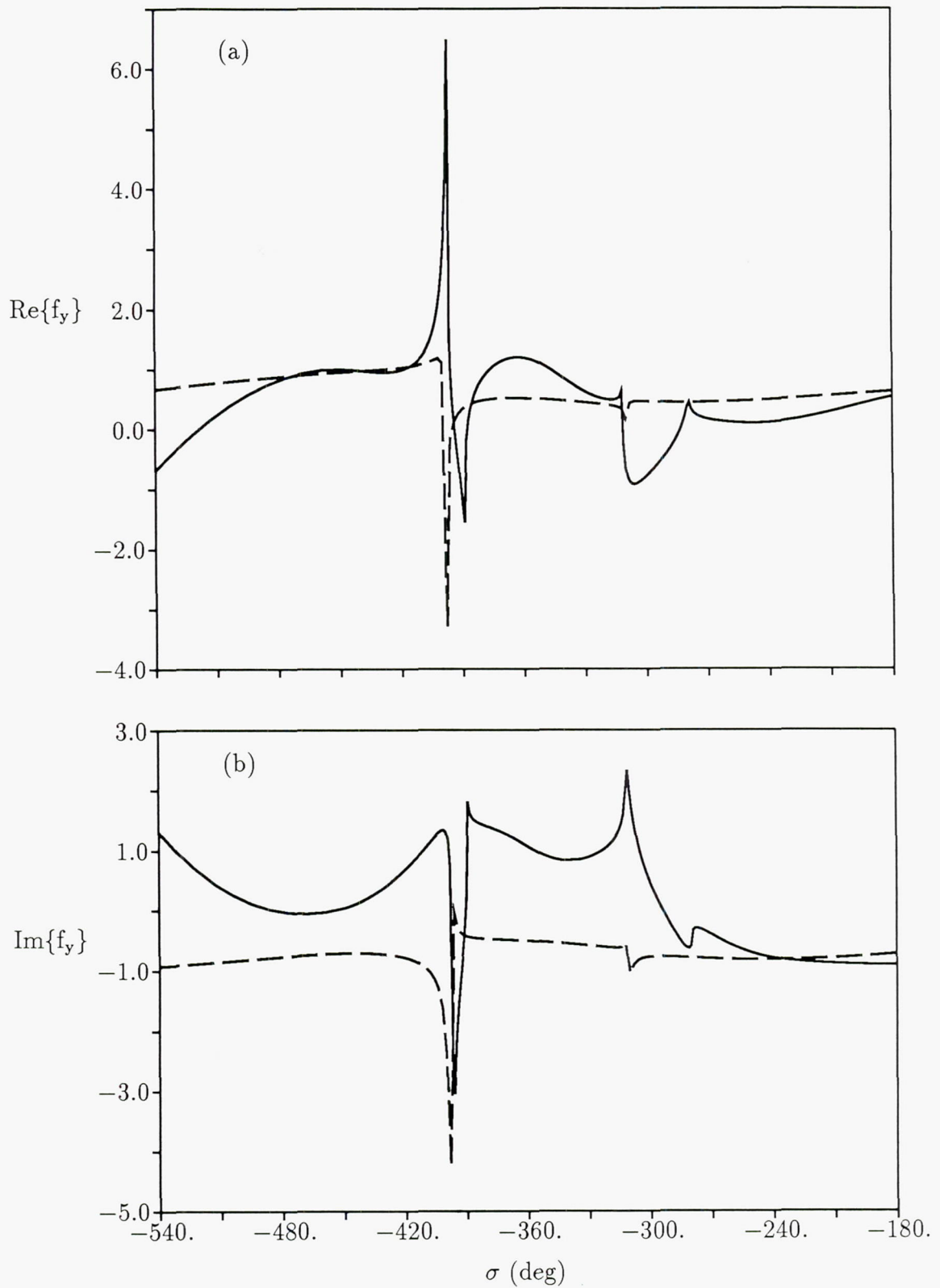
Figure 22. Unsteady lift versus interblade phase angle for the cambered NACA 0006 and corresponding flat-plate cascades subjected to incident vortical gusts with $v_g = (1,0)$ and $\omega = 5$: (a), (b), $---$ and ——— as in figure 21.

Figure 23. Mach number contours and surface Mach number distributions for steady flow with $M_{-\infty} = 0.19$ and $\Omega_{-\infty} = 45$ deg through the turbine cascade ($\Theta = 56.6$ deg and $G = 0.76$).

Figure 24. Contours of the real part of the unsteady vorticity for the turbine and the corresponding flat-plate (M = 0.19, $\Omega = \Theta = 45$ deg, G = 0.76) cascades subjected to an incident vortical gust with $v_g = (1, 0)$, $\omega = 5$ and $\sigma = -2\pi$.

Figure 25. Contours of the real part of the source term for the turbine and the corresponding flat-plate cascades subjected to an incident vortical gust with $\mathbf{v_g} = (1, 0)$, $\omega = 5$ and $\sigma = -2\pi$.

Figure 26. Contours of the in-phase component (real part) of the unsteady pressure for the turbine and the corresponding flat-plate cascades subjected to an incident vortical gust with $v_g = (1,0)$, $\omega = 5$ and $\sigma = -2\pi$.

Figure 27. Unsteady pressure-difference response for the turbine and corresponding flat-plate cascades subjected to an incident vortical gust with $v_g = (1,0)$, $\omega = 5$ and $\sigma = -2\pi$: (a) in-phase component (real part); (b) out-of-phase component (imaginary part); $- - -$ flat-plate cascade, ——— turbine cascade.

Figure 28. Unsteady lift versus interblade phase angle for the turbine and corresponding flat-plate cascades subjected to incident vortical gusts with $v_g = (1,0)$ and $\omega = 5$: (a), (b), – – – and ——— as in figure 27.

16. Abstract

A method for predicting the unsteady aerodynamic response of a cascade of airfoils to entropic, vortical, and acoustic gust excitations is being developed. Here, the unsteady flow is regarded as a small perturbation of a nonuniform isentropic and irrotational steady background flow. A splitting technique is used to decompose the linearized unsteady velocity into rotational and irrotational parts leading to equations for the complex amplitudes of the linearized unsteady entropy, rotational velocity, and velocity potential that are coupled only sequentially. The entropic and rotational velocity fluctuations are described by transport equations for which closed-form solutions in terms of the mean-flow drift and stream functions can be determined. The potential fluctuation is described by an inhomogeneous convected wave equation in which the source term depends on the rotational velocity field, and is determined using finite-difference procedures. In this report the analytical and numerical techniques used to determine the linearized unsteady flow are outlined. Results are presented to indicate the status of the solution procedure and to demonstrate the impact of blade geometry and mean blade loading on the aerodynamic response of cascades to vortical gust excitations. The analysis described herein leads to very efficient predictions of cascade unsteady aerodynamic response phenomena making it useful for turbomachinery aeroelastic and aeroacoustic design applications.